The Spectroscopy of Autoionising and Predissociating Rydberg States of NO

Douglas Thomas Charles Lazenby

UCL

A thesis submitted

in partial fulfilment of the requirements

for the degree of

Master of Philosophy

March 2011

Declaration

'I, Douglas Thomas Charles Lazenby, confirm that the work presented in this thesis is my own. Where information has been derived from other sources, I confirm that this has been indicated in the thesis.'

Acknowledgements

Firstly I'd like to extend my profound gratitude to Prof. Helen Fielding and Dr. Russell Minns. Their patience and support at points has been nothing short of remarkable - it's been a genuine pleasure working with such intelligent, personable people. I'd also like to thank the many members of the group that have come and gone since I've been here, for interesting discussions and answering my many questions about Rydberg states and science in general. A special mention also goes to the multitude of friends who've shared brief coffee breaks, slightly longer pint breaks, and nothing short of epic 'special times'. Daz, Dave, James, Christian, Adam and Pete - thanks.

Finally, I'd like to thank Dad and Diane for their endless support - I'm in no doubt that I wouldn't have finished without you.

And Russell, always remember that no matter how complicated it looks, maths is simple - you just need to write it down.

This thesis is based on the following publications:

Chapter 4

Interferences between competing ionisation and dissociation decay pathways in NO

D.T.C. Lazenby, R.S. Minns, F.H.J. Hall and H.H. Fielding

J. Phys. B-At. Mol. Opt. Phys. In preparation.

Chapter 5

The effect of vibrational excitation on the predissociation dynamics of the Rydberg states in NO

R.S. Minns, D.T.C. Lazenby, F.H.J. Hall1, R. Patel, N.J.A. Jones and H.H. Fielding

J. Phys. B-At. Mol. Opt. Phys. In preparation.

Abstract

We employ a 2-colour multi-photon excitation scheme to excite autoionising and predissociating Rydberg states of NO converging to the $v^+ = 1, N^+ = 0$ ionisation limit of the molecular ion *via* the $A^2\Sigma^+ |v' = 1, N' = 0\rangle$ intermediate. In this energy region there is competition between autoionisation and predissociation and we monitor the fragments from both decay processes in an effort to study such competition; the NO^+ ions from the ionisation route are detected directly and a second (2+1) REMPI scheme is used to probe the $N(^2D)$ dissociation product. By least squares fitting of the Fano formula to the experimental data we derive linewidths, Γ, shape indexes, q, and lifetimes, τ, for selected resonances from the dominant np(0) and nf(2) Rydberg series present and assess qualitatively the variation in each throughout the spectrum. At several points in the spectrum where there is near resonance between the many Rydberg series present, we observe interferences between the decay pathways in which increased flux through one channel is accompanied by suppression in the other. The experimental data recorded here is studied alongside earlier work in the group on Rydberg states converging to the $v^+ = 0, N^+ = 0$ ionisation limit where dissociation is the only available (non-radiative) decay path. By least-squares fitting of the Fano formula to the experimental data, linewidths are derived and the effect of a vibrationally active core upon the predissociation dynamics is investigated.

Contents

List of Figures

List of Tables

Chapter 1

Introduction

Diatomic Rydberg systems are attractive systems to work with for a number of reasons. One of the major advantages is that, though they possess only a single molecular bond, diatomic Rydberg molecules possess many of the characteristics of complex molecular systems including: strong non-adiabatic couplings between electronic and nuclear motion, energy flow between different degrees of freedom (electronic, vibrational, rotational), delicately balanced interference effects between competing non-radiative decay pathways, complex resonances and internal time-scales spanning orders of magnitude. Thus, the introduction of nuclear degrees of freedom into a Rydberg system renders even a two atom Rydberg molecule a challenge to describe fully. While the full quantum mechanical characterisation of such a many bodied system is currently impossible, a huge amount of progress has been made in terms of elucidating the energetic structure and dynamical behaviour of the excited states of diatomic Rydberg molecules. Such progress has brought greater understanding of these ostensibly simple systems and, with it, comes a shift from simple characterisation, to control. From the perspective of the current work, exhibiting control on a diatomic system in an intuitive manner, with knowledge of the various phase parameters integral to such control, points the way to developing an intuition with regard to the control of larger, more chemically interesting molecules. As will be discussed shortly, many

control schemes are based on the interferences between different molecular pathways, and the final state distribution is highly dependent on the excited state dynamics of the quantum states involved. A detailed knowledge of the dynamical behaviour of the molecule in the energy range of interest is, therefore, essential prior to the construction of a control scheme. The work presented here goes some way towards this goal.

1.1 Rydberg States

In 1890, Rydberg produced a mathematical formula correctly predicting the wavenumbers of all of the observed emission lines of hydrogen:

$$\tilde{\nu}_{n_1 n_2} = R_{\mathrm{H}}\Big(\frac{1}{n_1^2} - \frac{1}{n_2^2}\Big) \tag{1.1}$$

Here, n_1 and n_2 are integers with $n_2 > n_1$. Each series of lines has a common lower member and the series members are obtained by fixing n_1 and allowing n_2 to vary (*e.g.* $n_1 = 1$ for the Lyman series, $n_1 = 2$ for the Balmer series *etc.*). R_{H} is a constant equal to 109768 cm^{-1} and corresponds to the ionisation potential of the hydrogen atom. Equation (1.1) was deduced empirically from experimental observation but the physical significance of the electronically excited, high-n states (or Rydberg states) was not realised until Bohr proposed his model of the hydrogen atom in 1913. The Rydberg electron is in a relatively large orbit about the rest of the molecule and spends much of its time at the outer periphery seeing, on average, only the single positive charge of the rest of the system. It follows that, to a first approximation at least, the electron moves in a purely Coulombic potential and thus Rydberg states behave very much as do the excited states of the hydrogen atom. Though not without shortcomings, the Bohr model of the hydrogen atom succinctly encapsulates the interesting characteristics of Rydberg states and as such it is included, in brief, here.

Bohr proposed that the electron (or Rydberg electron) moved in circular orbits

about an infinitely heavy nucleus of charge Ze. In contrast to classical mechanics, such orbits exist only at certain allowed energies, E_i, and the electron does not radiate unless it makes a transition between these orbits. The circular motion is provided by the electrostatic attraction between the nucleus and the electron and thus

$$\frac{Ze^2}{4\pi\epsilon_0 r^2} = \frac{mv^2}{r}. \tag{1.2}$$

Here, Z is the atomic number, e the elementary unit of charge, ϵ_0 the permittivity of free space, m the mass of the electron, v the linear velocity of the electron and r the orbital radius. Bohr placed a further restriction on the model so that, in addition to the quantisation of the energy of the system, the angular momentum, L, was also quantised in units of $\hbar = h/2\pi$ such that

$$L = mvr = n\hbar \tag{1.3}$$

where n is an integer greater than or equal to one. The introduction of n discretises the allowed energies and for this reason it is known as the *principal* quantum number. From equations (1.2) and (1.3) we have the orbital radius,

$$r = \frac{4\pi\epsilon_0\hbar^2}{Ze^2m}n^2, \tag{1.4}$$

and the velocity,

$$v = \frac{Ze^2}{4\pi\epsilon_0\hbar}\frac{1}{n}. \tag{1.5}$$

Choosing the zero of energy such that $E = 0$ when the electron is at rest and completely separated from the nucleus, the total energy is the sum of the kinetic energy, T, and the potential energy, V,

$$E_n = T + V = \frac{1}{2}mv^2 - \frac{Ze^2}{4\pi\epsilon_0 r} = -\frac{m}{2}\Big(\frac{Ze^2}{4\pi\epsilon_0\hbar}\Big)^2\frac{1}{n^2}. \tag{1.6}$$

The subscript labels the n-th state, of energy E_n, while the negative sign indicates that the electron is bound to the nucleus.

Thus, the energy of radiation emitted due to a transition from state j to state i with $E_{\mathrm{j}} > E_{\mathrm{i}}$ is given by

$$E_{\mathrm{ij}} = \frac{m}{2}\Big(\frac{Ze^2}{4\pi\epsilon_0\hbar}\Big)^2\Big(\frac{1}{n_{\mathrm{i}}} - \frac{1}{n_{\mathrm{j}}}\Big). \tag{1.7}$$

Comparison with equation (1.1) therefore yields

$$R_\infty = \frac{m}{2}\Big(\frac{Ze^2}{4\pi\epsilon_0\hbar}\Big)^2. \tag{1.8}$$

This retrieves a value of $R_\infty = 109737\ \mathrm{cm}^{-1}$ in good, but not perfect, agreement with the experimentally determined Rydberg constant for hydrogen, R_{H}. This error is accounted for by recognition of the finite mass of the nucleus; in the case of the hydrogen atom, a single proton. Equation (1.8) is modified so that, for a species, X, with a core of mass, M,

$$R_{\mathrm{X}} = \frac{\mu}{2}\Big(\frac{Ze^2}{4\pi\epsilon_0\hbar}\Big)^2 \tag{1.9}$$

where the reduced mass, μ, is given by

$$\mu = \frac{mM}{m+M} \tag{1.10}$$

and simply accounts for the fact that the Rydberg electron and the rest of the molecule orbit about a common centre of mass. This recovers the experimentally observed ionisation potential of the hydrogen atom. We note at this point that R_{X} is simply related to R_∞ through

$$R_{\mathrm{X}} = \frac{R_\infty}{1+m/M}. \tag{1.11}$$

From a spectroscopic perspective, the great achievement of the Bohr theory of the atom is that it derived Rydberg's constant in terms of fundamental constants. For

the present discussion however, it illustrates many of the characteristics of Rydberg systems which make them interesting. One of the relatively unique aspects of Rydberg states is their regularity - virtually all observable phenomena display a dependence upon the principal quantum number and the Bohr model provides information on how the properties vary with n; some of these scaling laws are given in table 1.1. Equation (1.4) shows that the orbital radii scale as n^2 and equation (1.6) that their binding energy goes as n^{-2}; thus they occupy large, loosely bound orbits. Note that a consequence of the scaling of the radius leads to a large geometric cross-section, in proportion with n^4. The classical orbital period is proportional to n^3 and is of the order of 10^{-11} s for $n = 40$. This is longer than the characteristic period of a typical vibration and similar to that of the rotational period of a small molecule. In the context of a molecule this becomes very important - the Born-Oppenheimer approximation no longer holds and the motion of the electron no longer adjusts rapidly to that of the vibrating and rotating nuclei. The polarisability of a Rydberg state scales as n^7 [2] indicating that such states are perturbed by even modest external fields. Another important characteristic of Rydberg states is the electronic degeneracy: for each value of n, the orbital angular momentum quantum number, l, takes values from zero to $n-1$ and for each of these the magnetic quantum number, m_l, takes integer values in the range $-l$ to $+l$ [3]. It is easy to verify that this adds up to an n^2 electronic degeneracy, or 1600 states for $n = 40$. The energy spacing between adjacent states goes as n^{-3} so at $n = 40$ there are already several hundred states per wavenumber.

An important consequence of the rapid convergence of the energy level spacing between adjacent states is that the output of a broad bandwidth laser pulse can excite a set of Rydberg states coherently; this is known as a wavepacket. Mathematically such a superposition may be expressed as

Property	**Scaling**	$n = 1$	$n = 40$
Binding Energy	n^{-2}	109768 cm^{-1}	69 cm^{-1}
Energy Spacing	n^{-3}	82258 cm^{-1}	3 cm^{-1}
Orbital Radius	n^2	0.53 Å	850 Å
Orbital Period	n^3	150 as	10 ps
Electronic Degeneracy	n^2	1 state	1600 states

Table 1.1: Scaling properties of Rydberg electrons as derived from the Bohr model

$$|\Psi(r,t)\rangle = \sum_n c_n \, |\psi_n(r)\rangle \, \mathrm{e}^{-iE_n t} \tag{1.12}$$

where c_n, E_n and $|\psi_n(r)\rangle$ respectively denote the amplitude, energy and time independent radial wavefunction of the n-th Rydberg state. Wavepackets provoke a great deal of interest since they display both classical and non-classical behaviour - at short times the wave packet behaves like a classical electron in a Kepler orbit and oscillates between the inner turning point (in the core region) and outer turning point [4]. At longer times, the wavepacket becomes dispersed due to the anharmonicity of the potential and its quantum nature manifests as full and partial revivals [5]. In particular, the interferences between wavepackets are of interest since these may be manipulated to control the long term dynamics (see section 1.3).

Rydberg series are by no means only confined to hydrogenic systems. They have been observed in many electron atoms as well as large molecules [6–8] and, more recently, in an unusual He nanodroplet system [9]. In addition, coherent control (see section 1.3) has been demonstrated in phosphorus-doped silicon [10] in the solid phase. In principle, any compact, charged assembly can exhibit Rydberg series conditional upon the fact that the charged core remains intact (*i.e.* it is stable) and that the

Rydberg wavefunctions have enough space to expand into. As noted above, Rydberg series of any system may be considered as excited states of the hydrogen atom and, as such, the Rydberg electron moves in a Coulomb potential; this immediately precludes the occurrence of Rydberg series in anionic systems since the excited electron will see a neutral core. It is a remarkable fact that the Rydberg series in *all* non-hydrogenic systems can be fitted to the equation

$$\begin{aligned} E_{\upsilon^+N^+nl} &= I_{\upsilon^+N^+} - \frac{R_{\mathrm{X}}}{\nu_l^2} \\ &= I_{\upsilon^+N^+} - \frac{R_{\mathrm{X}}}{(n-\mu_l)^2}. \end{aligned} \tag{1.13}$$

Here, $I_{\upsilon^+N^+}$ is the ionisation potential of the core in the rovibrational quantum state $\{\upsilon^+N^+\}$, where υ^+ and N^+ are vibrational and rotational quantum numbers respectively. The quantity $\nu_l = n - \mu_l$ is the effective principal quantum number and can be thought of simply as a measure of the energy of the Rydberg state. Note that the form of equation (1.13) is identical to that of equation (1.6) up to the addition of a constant and the introduction of the quantum defect, μ_l.

The quantum defect was introduced empirically in an effort to describe the shift in energy levels of the alkali metals relative to equation (1.6) and the subscript l indicates that its value is found to be highly dependent on the orbital angular momentum of the Rydberg electron; the relative magnitude of a set of quantum defects broadly goes as $\mu_{\mathrm{s}} > \mu_{\mathrm{p}} > \mu_{\mathrm{d}}$, with $l \geq 3$ being nearly zero. However, this somewhat understates the importance of the quantum defect from the perspective of Rydberg systems. The radial wavefunction of a Rydberg electron is strongly peaked at the outer periphery of its orbit so that for the majority of the time the electron sees the single net positive charge from the rest of the molecule and therefore may be treated as a pseudo one-electron system. That said, *all* radial wavefunctions have some probability amplitude inside the core region where the electron feels the complicated potential due to the rest

of the system. These many-body interactions are parameterised by a single constant[1], μ_l, and manifest in Rydberg spectra as a shift in the energy levels relative to that of the hydrogen atom (see section 1.2). It follows that this shift is likely to be larger for wavefunctions that are more strongly peaked near to the ionic core and these are the low orbital angular momentum states, hence the subscript l on the quantum defect.

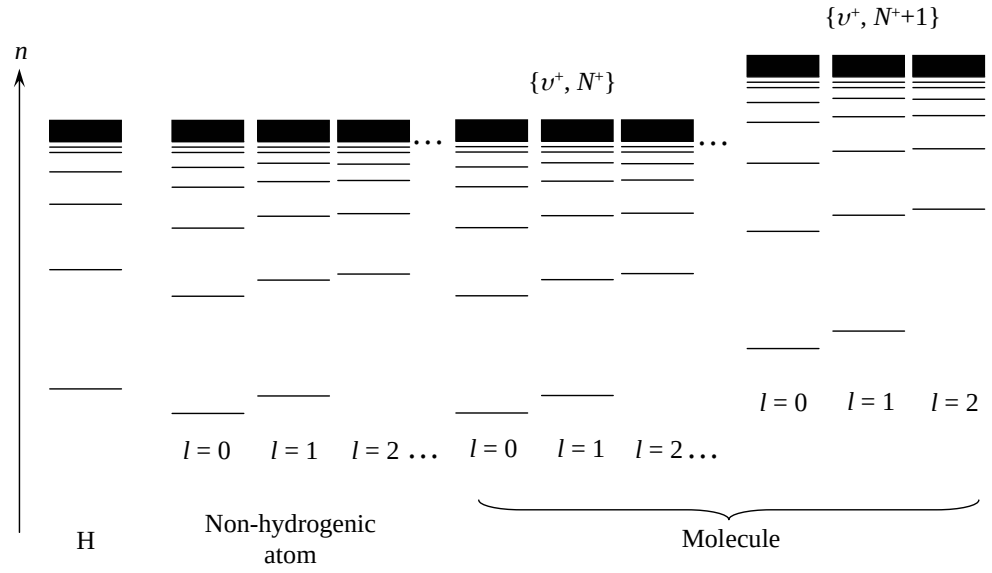

Figure 1.1: Illustration of the channel structure in Rydberg molecules. The presence of the core electrons in non-hydrogenic systems shifts the energy levels relative to those of the hydrogen atom. The presence of a vibrating and rotating core complicates this further such that each rovibrational state of the core supports a set of Rydberg series.

The energetic structure of Rydberg series in a number of systems is illustrated schematically in figure 1.1. In the hydrogen atom, states of the same n but different l and m_l are degenerate. In non-hydrogenic atoms the interaction of the Rydberg electron with the core lifts this degeneracy and shifts the energies of the states relative to those of hydrogen. In a molecular system the core vibrates and rotates and this

[1]To a good approximation μ_l is constant across a series. In fact it varies weakly with energy and this is more pronounced at low-n where the Rydberg character is reduced due to the proximity of the core.

affects the Rydberg electron when it is nearby; thus each rovibrational state of the core supports a set of Rydberg series, each characterised by a quantum defect. Note that in this case it is clear that the bound states of one Rydberg series may be degenerate with the ionisation continua of one or more other Rydberg series - this leads to a wavefunction of mixed discrete-continuous character, the consequences of which will be discussed shortly.

1.2 Multichannel Quantum Defect Theory

The empirical observation that the energy of a Rydberg state in a non-hydrogenic system is shifted from that of hydrogen by a constant value allows us to successfully fit the energy levels of all of the members of a given Rydberg series to a simple formula. It is the task of theory to explain this fact and to extract an appropriate wavefunction such that the quantum defect is constant (or nearly constant) with n, a task elegantly accomplished by quantum defect theory (QDT). QDT treats the bound states along with the adjoining ionisation continuum as a single entity allowing us to define them as an excitation *channel* - consideration of the simple, single channel problem yields great insight into the nature of the quantum defect and the applicability of QDT while also offering a view to extend the theory to a more realistic, many-channel system such as is encountered in the nitric oxide molecule.

The theoretical approach hinges on a central assumption that the physics of the system can be separated into two distinct regions: a short range region ($r < r_c$) where the Rydberg electron experiences a complex potential due to the rest of the molecule, and a longe range region ($r > r_c$) where the electron moves in a purely Coulombic potential. Consider then, a system in an electronically excited state (*i.e.* a Rydberg state) of energy, in atomic units, given by

$$E = -\frac{1}{2\nu^2}. \tag{1.14}$$

In the outer region where the electron is moving in a purely Coulombic potential the Schrödinger equation reduces to

$$\left[\frac{\mathrm{d}^2}{\mathrm{d}r^2} + \left(2E + \frac{2}{r} - \frac{l(l+1)}{r^2}\right)\right]\psi_l(\nu, r) = 0. \tag{1.15}$$

Equation (1.15) has been studied extensively (*e.g.* [11]) and its solution is well known to be the linearly independent pair of regular and irregular Coulomb functions, denoted $f_l(\nu, r)$ and $g_l(\nu, r)$ respectively. The names indicate the differing behaviour of the two functions near the origin, that being

$$f_l(\nu, r) \sim r^{l+1} \qquad \text{and} \qquad g_l(\nu, r) \sim r^{-l} \qquad \text{for} \qquad r \to 0 \tag{1.16}$$

i.e. $f_l(\nu, r)$ remains finite at the origin (hence *regular*) and $g_l(\nu, r)$ is divergent at the origin (hence *irregular*). The boundary condition for atomic hydrogen is that the wavefunction remains finite at all radial distances and thus the solution, in this case, retains $f_l(\nu, r)$ while discarding $g_l(\nu, r)$. In the case of a polyelectronic system, however, we consider only the part of the problem that lies outside the influence of the core at distances $r > r_c$; consequently, we retain the irregular function in our general solution. This has the form

$$\psi_l(\nu, r) = c_f f_l(\nu, r) + c_g g_l(\nu, r), \qquad r > r_c \tag{1.17}$$

where c_f and c_g are weighting constants to be determined from the boundary conditions but are often written as $c_f = +\cos(\pi\mu_l)$ and $c_g = -\sin(\pi\mu_l)$. There are two points to note about this choice for the constants. Firstly, they ensure that the wavefunction is normalised such that $|c_f|^2 + |c_g|^2 = 1$, and secondly the relative weighting of the functions depends solely on the constant μ_l. If $\mu_l = 1/2$ then only g contributes, whereas for $\mu_l = 0$ only f contributes, as is the case for hydrogen.

For bound states we require the wavefunction to vanish for $r \to \infty$. The asymptotic form of the Coulomb functions is

$$\begin{aligned} f(\nu, r \to \infty) \quad &\to \quad C(r)\sin(\pi(\nu - l))\mathrm{e}^{r/\nu} \\ g(\nu, r \to \infty) \quad &\to -C(r)\cos(\pi(\nu - l))\mathrm{e}^{r/\nu}, \end{aligned} \tag{1.18}$$

where $C(r)$ is a function that goes to zero more slowly than the exponential function blows up. In the asymptotic limit therefore, the radial wavefunction must satisfy

$$\psi_l(\nu, r \to \infty) \to C(r)[\cos\pi\mu_l \sin\pi(\nu - l) + \sin\pi\mu_l \cos\pi(\nu - l)]\mathrm{e}^{r/\nu} = 0, \tag{1.19}$$

which is true if the term in square brackets is null. Using standard trigonometric identities and with the knowledge that l is an integer, this condition reduces to

$$\sin\pi(\nu + \mu_l) = 0, \tag{1.20}$$

which is satisfied for $\nu + \mu_l = n = 0, \pm1, \pm2....$ At this point we recognise n as the principal quantum number for which $n = l + 1, l + 2, ...$ and clearly $\nu = n - \mu_l$. We thus recover the Rydberg equation and see that the quantum defect shifts the energies of a Rydberg state relative to atomic hydrogen.

It should be noted that the wavefunction is energy independent and the energy parameterisation by ν is a consequence of imposing the boundary conditions at the final stage. It is this fact which allows the wavefunction to describe the whole Rydberg series for a given orbital angular momentum, l, as well as the continuum beyond. Hence, each Rydberg series, along with its associated continuum, is termed a *channel*. In addition, the form of the deduced wavefunction differs from that of hydrogen by the inclusion of the irregular Coulomb function, $g_l(\nu, r)$. Mathematically, this means that the nodes of the function depend not only on n but also on the quantum defect and this gives an indication of the physical interpretation of μ_l. As the series limit is approached, the bound state wavefunction acquires more nodes, thus becoming more oscillatory and tending to the wavefunction of the continuum. This has the

effect that as n increases, all but the outermost nodes become stable and are said to *recapitulate*. The positions of the nodes are related to the phase in the continuum since the wavefunction must change smoothly into that of a free electron wavefunction as the series limit is passed, and the condition for recapitulation is that μ_l must be a constant. It follows then, that as long as μ_l is nearly a constant with energy, which is true for high n Rydberg states, we can consider it to be a phase shift in the radial function with respect to that of hydrogen [12].

It is important to note that in QDT the interaction of the electron with the core is considered as a collision. The details of this are controlled by the short range interaction when the electron is in the core region and therefore μ_l is strongly dependent on the level of penetration of the core by the electron, *i.e.* how much of the radial wavefunction is located at distances $r < r_c$. This is clearly dependent on the orbital angular momentum of the electron and hence, we see a decrease in the value of μ_l from s states to higher angular momentum states, where the level of penetration is reduced.

In NO, and indeed any molecule, we must also deal with the complications associated with the vibrating and rotating core. As described in section 1.1, each rovibrational state of the ionic core supports a set of Rydberg series and their adjoining continua. Thus a molecular system is composed of many channels and the theory must be extended to account for this and the interactions between them - this is multichannel quantum defect theory (MQDT) [13]. The multichannel formulation of QDT is similar to that described above for a single channel system. The space of the molecule is split into two regions, an inner region where the Rydberg electron feels the complex potential due to the core, and an outer region where it feels a Coulombic potential. Again, the asymptotic behaviour of the radial function is described by a superposition of regular and irregular Coulomb functions and the relative weighting of these is controlled by the level of interaction between the electron and the core. In the molecular case however, the electron will experience a different core poten-

tial depending on the rovibrational state of the core at the time of the collision and hence the quantum defect is now a function of the internuclear separation, R. The collision of the electron and the ionic core happens on an extremely fast timescale as a consequence of the high speed achieved by the electron as it accelerates in the Coulomb potential. It follows that, for the duration of the collision, the electron sees a fixed core, that is one with a constant internuclear separation. Hence as opposed to one quantum defect, we now have a set; one for each value of R. In addition, for molecular systems it is necessary to incorporate the possibility that the ionic core may be in an excited (*e.g.* electronically/ vibrationally/rotationally) state and therefore that the Rydberg electron can be in one of many channels. Interactions between these channels occur in the core region and these short-range interactions can lead to transitions between channels - it is these interactions that give rise to autoionisation and predissociation. In MQDT these interactions are modelled as a scattering of the Rydberg electron with the ionic core and this scattering process is described by a matrix known as the reaction, or K, matrix. One way to understand this is that the Rydberg electron arrives in the core region in a well-defined quantum state and interacts with the core, thereby exchanging energy and angular momentum. As a result of the collision, the Rydberg electron emerges from the core region with different quantum numbers and the quantum state of the core has also changed. In other words, the K-matrix determines the admixture of regular-irregular character of the outgoing wave and is thus closely related to the quantum defects [14].

Through extensions of the method described above it is possible to predict diatomic spectra that reproduce interchannel couplings, photoionisation, predissociation and autoionisation with impressive correlation with experimental data (*e.g.* [15, 16]). In particular, derivation of the channel wavefunctions and long-range quantum defects has implications for the construction of coherent control schemes based around wave-packet interferometry (see section 1.3).

1.3 Coherent Control

Coherent control [17] describes the field of science in which optical methods are used to control atomic and molecular processes. Further from simply attempting to elucidate the nature of fundamental interactions between light and matter, coherent control aims, ultimately, to control the products of photochemical reactions.

Types of coherent control scheme generally fall into two categories: control in the frequency domain and control in the time domain. One frequency domain approach based on the interference between two narrow bandwidth lasers was proposed by Brumer and Shapiro in 1986 and is illustrated in figure 1.2. Consider a three state system with two optical pathways to ionisation or dissociation ($|i\rangle$ and $|d\rangle$ in figure 1.2); a three photon process or a single photon of the third harmonic. The probability of population transfer to either state depends on the square of the coherent sum between the two pathways, from which we obtain an interference term for the ionisation process with an associated phase δ_{i}. Similarly for the dissociative process we have an associated phase δ_{d}. When the two are not equal (*i.e.* the phase-lag, $\delta = |\delta_{\mathrm{i}} - \delta_{\mathrm{d}}| \neq 0$), then it is possible to enhance one pathway at the expense of the other. When $\delta = \pi$ we have a system in which maximum control can be achieved [18] since in this case the phase required to maximise signal in one channel is also the phase required to minimise signal in the other. The Brumer-Shapiro method was first demonstrated experimentally by Gordon and co-workers in 1991 where they controlled dissociation and ionisation in DI [19] and has since been employed to control numerous processes including the ionisation of mercury [20] as well as the photoionisation and photodissociation of HI [21].

Another frequency domain method is the Stimulated Raman Adiabatic Passage (STIRAP) method which can result in 100% transfer efficiency. This is illustrated schematically in figure 1.3. The aim is to transfer as much population from state $|1\rangle$ to state $|3\rangle$ as possible. State $|2\rangle$ is optically coupled to state $|1\rangle$ and $|3\rangle$ and

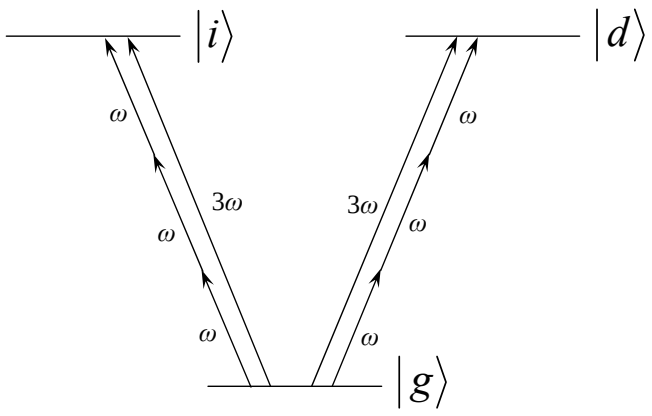

Figure 1.2: Schematic illustrating the Brumer-Shapiro method. By controlling the relative phases of the ionisation/dissociation pathways it is possible to selectively enhance one product over the other.

decays by spontaneous emission, therefore population in $|2\rangle$ would lead to a loss in transfer efficiency. In order to circumvent this, the population of $|2\rangle$ is kept to a minimum throughout the experiment in the following way: first, pulse ω_{23} couples $|2\rangle$ and $|3\rangle$ creating a so-called 'dressed' state. Then ω_{12} couples $|1\rangle$ to the dressed state. Figure 1.3(b) shows the relative timing of the pulses. By turning off pulse ω_{23} before ω_{12}, the population in $|3\rangle$ cannot decay back to $|1\rangle$ *via* $|2\rangle$. The presence of both fields adiabatically couples $|1\rangle$ to $|3\rangle$ and in this way 100% transfer efficiency may be achieved. The STIRAP method has been demonstrated in a variety of systems from atoms [22, 23] to larger systems [24].

Time domain schemes were first discussed by Tannor, Koslof and Rice [25, 26]. As mentioned earlier, the output from a broad bandwidth picosecond or femtosecond laser can be used to excite several states coherently, forming a wavepacket. The excited wavepacket evolves in time over some potential surface and application of another optical pulse can either pump or dump it onto another surface. The time delay between excitation of the wavepacket and the arrival of the second optical pulse can be used to demonstrate selectivity over which potential surfaces are accessible

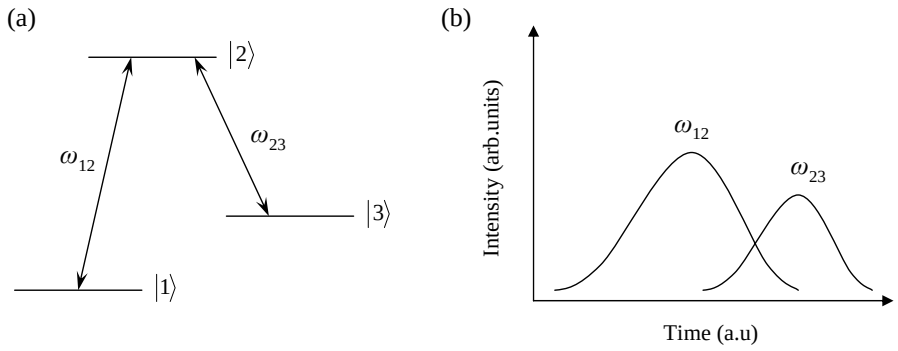

Figure 1.3: Schematic illustrating the STIRAP method. Figure (a) gives the energy diagram and (b) gives the relative pulse timings. Initially a pulse, ω_{23}, arrives coupling states $|2\rangle$ and $|3\rangle$ to form a dressed state. After a delay, a second pulse, ω_{12}, arrives coupling state $|1\rangle$ to the dressed state. In this way population is transferred adiabatically from $|1\rangle$ to $|3\rangle$. Turning ω_{23} off before the second pulse arrives prevents transfer from $|3\rangle$ to $|1\rangle$ *via* $|2\rangle$.

and therefore selectivity over the final products. Baumert *et al* [27] demonstrated control over the sodium dimer by exciting a vibrational wavepacket and then ionising the system after some delay. After excitation, the wavepacket oscillates between the classical turning points. It was seen that when the wavepacket was at the inner turning point the ionising pulse produced Na_2^+, whereas if the wavepacket was at the outer turning point, Na^+ was produced. This scheme has also been utilised to control bimolecular reactions of Xe with molecular iodine [28].

Another technique used to great effect is pulse-shaping. This technique controls the phase, amplitude and polarisation of broad bandwidth, femtosecond light pulses, and through this manipulates the composition and dynamics of the wavepackets produced. This method has tended to rely on feed-back controlled learning algorithms to optimise the characteristics of the light pulse in order to obtain the maximum of the desired product. The sample is exposed to random pulse shapes and the products of the photochemical reaction detected. The pulses that best perform the chosen

control task (*i.e.* the pulses which generate the highest yield of the desired product or enhance the population in a required final state) are kept while the others are discarded. These are then bred to form a new generation and the process is repeated until optimal control over the desired product is attained. This technique has had remarkable results in demonstrating control over a variety of systems from atoms to biological systems [29, 30].

Another important method of coherent control is based around the interference between wavepackets. Typically, a train of two or more phase-related femtosecond pulses are used to excite two or more wavepackets in an atom or molecule. The optical amplitudes and phases are imprinted onto the quantum amplitudes and phases of the wavepackets, and by controlling the relative phase of the optical pulses it is possible to selectively induce constructive or destructive interference - this is wavepacket interferometry. Fleming and coworkers were the first to demonstrate this scheme to selectively induce constructive or destructive interference in vibrational wavepackets in iodine [31, 32]. Interfering wavepackets have since been used to demonstrate Young's double-slit experiment in an atom [33], to construct Schrödinger's Cat states [34] and to control the orbital angular momentum composition of a wavepacket with mixed angular momentum character [35]. More recently Katsuki *et al* [36, 37] have reconstructed the spatiotemporal evolution of quantum interferences between vibrational wavepackets in the iodine molecule. In this case, two counterpropogating wavepackets are generated using a pair of phase-locked femtosecond pulses whose relative phase is locked to within an attosecond timescale. The wavepackets overlap periodically and transient picometric standing waves appear as so-called 'quantum ripples'. In order to visualise this the quantum ripple is excited to another potential surface whereby the flourescence intensity is measured as a function of the probe delay and wavelength - this creates a space-time image (or quantum carpet) of picometer and femtosecond resolutions that can be actively tailored through the precise tuning of the relative phase of the two wavepackets.

In our own group, control has been exerted over the rotational angular momentum of electronic wavepackets in atoms and molecules [35,38] and also on dissociating and autoionising Rydberg electron wavepackets in NO [39].

1.4 Summary

This chapter has introduced Rydberg molecules and some of their more interesting characteristics. In addition, the theoretical framework for describing Rydberg systems (MQDT) has been briefly described and various coherent control schemes discussed. From the perspective of coherent control, Rydberg molecules are attractive systems. Since a diatomic molecule both vibrates and rotates, all of the sources of molecular phase present in a larger molecule are also present in a diatomic Rydberg molecule. Knowledge of the molecular phase, and how this can be manipulated by the optical phase, is imperative for the design of intuitive control schemes, and in a Rydberg molecule it is relatively simple to see where this phase originates from. In terms of wave-packet inteferometry experiments, the accurate manipulation of an excited wavepacket hinges on knowledge of the phase relationships between the various components of the wavepacket and thus on the excited state dynamics of the individual constituents - thus investigation into such processes in NO has broad relevance for coherent control of this molecule.

The rest of this thesis is organised as follows. Chapter 2 introduces NO, previous spectroscopic work on the molecule and the methods used in analysis of the experimental data. Chapter 3 outlines the experimental equipment and techniques relevant to the work presented in this thesis. Chapter 4 presents spectroscopy of Rydberg states converging to the $\upsilon^+ = 1$ ionisation threshold and identifies regions of the spectrum where there are interferences between competing non-radiative ionisation and dissociation decay channels. Chapter 5 takes previous work that recorded spectra of Rydberg states converging to the $\upsilon^+ = 0$ ionisation limit and draws a comparison

between the decay dynamics of Rydberg series based on a vibrating and vibrationless core. Chapter 6 summarises the work and provides an outlook for future experiments.

Chapter 2

Spectroscopy of NO

Nitric oxide is an ideal system in which to study molecular Rydberg states. It has a relatively low ionisation potential and Rydberg states that are easily accessible from the ground state in a one or two photon process. Excitation of a Rydberg electron leaves behind a stable, closed shell ionic core which simplifies theoretical treatments substantially. Furthermore, the unified framework provided by MQDT, employed alongside the considerable experimental work undertaken, has provided numerous complimentary experimental and theoretical studies over a wide range of energies. This has resulted in a wealth of accurate spectroscopic data along with a detailed knowledge of the energetic structure, the various couplings between Rydberg series and with valence states, and great insight into the understanding of molecular decay mechanisms.

NO has been studied extensively over the past five decades. Initial absorption spectroscopy by Miescher and co-workers led to the assignment of Rydberg series and provided ionisation potentials along with the first calculations of quantum defects for low l states [40–44]. A significant obstacle to progress was that the absorbtion spectra recorded were congested and correspondingly difficult to analyse. This difficulty was circumvented with the advent of multi-photon excitation schemes. A single photon excites a specific rovibrational level of an intermediate state and a second is used to

access the Rydberg states; the allowed transitions in the second phase of excitation are governed by single photon selection rules which restrict the number of final states accessed thereby reducing congestion whilst allowing greater selectivity over the accessed states. Multi photon excitation schemes have been used to great effect by various groups to probe highly excited Rydberg states above the first ionisation limit to divulge information pertaining to, amongst other things, ionisation potentials [45] the competition between rotational autoionisation and predissociation [46], the assignment of Rydberg series and calculation of quantum defects [47] and quantum interferences [48].

The approach used in this work to investigate predissociating Rydberg states was pioneered by Fujii and Morita through a series of papers in the early 1990s. A multiphoton excitation scheme was used to access Rydberg states *via* an intermediate which then decayed through autoionisation and predissociation. The NO^+ from the ionising decay was detected directly, whereas a second resonance enhanced multiphoton ionisation (REMPI) scheme was employed to ionise the nitrogen fragment from the predissociation process. The REMPI process was tuned to ionise either the N(^{2}D) or the N(^{4}S) fragment, thus obtaining information regarding coupling between Rydberg states and the valence states into which they decay. The research was extensive and provided unequivocal evidence that the decay dynamics of the np($\upsilon^+ = 0$) states are dominated by predissociation as opposed to rotational autoionisation [49] and that the predissociation yields of members of the s, p, and f ($n = 8 - 17$) series based on a vibrating core are strongly dependent on the energy and quantum numbers (n, l) of the Rydberg electron [50]. In addition, a detailed study of the 7f($\upsilon^+ = 1$) state showed that the decay of this state is chiefly governed by direct coupling to $^2\Sigma^+$ valence states ($I^2\Sigma^+$ and $A'^2\Sigma^+$ for the N(^{2}D) and N(^{4}S) fragments, respectively) [51] thereby indicating the importance of predissociation in the decay dynamics of nf states. A subsequent study of the region above the first ionisation limit where there is competition between autoionisation and predissociation showed

that the $np(v^+ = 1)$ states are dominated by predissociation while the $ns(v^+ = 1)$ are dominated by autoionisation [52]. A later study also indicated that even in g Rydberg states there are autoionising and predissociating processes that dominate over radiative decay [53].

There have been several experimental investigations on the bound states of NO using pulsed-field ionisation [54–56] and two-colour resonant four-wave mixing [57,58] as well as a series of investigations into the Stark effect in bound [55], predissociating [59, 60] and autoionising [61, 62] Rydberg states with corresponding theoretical analyses through matrix diagonalisation methods and/or MQDT. In part due to the wealth of experimental data available for NO, there have been a number of theoretical studies both below the first ionisation limit [63, 64], where predissociation is the only available fragmentation pathway, and above, where there is competition between ionisation and predissociation [16, 65]. In addition, the partial wave composition of the low-n Rydberg states has been calculated along with transition moments over a wide range of energies [66–68]. Some of the subtler complications of the spectra have been shown to be due to the strong s-d mixing in NO [69, 70] and NO has also been treated theoretically using R-matrix methods [71, 72].

Significant work has also been accomplished in our group with regard to the dynamics of the Rydberg states of NO in the region where ionisation and dissociation compete. For example, Minns *et al* demonstrated control over the ionisation:dissociation branching ratio through determination of the accumulated phase-difference between various components of an excited wavepacket; a sequence of phase-locked optical pulses were then employed to selectively enhance or depopulate the Rydberg population [38]. Previous work has elucidated the importance of the relative phase difference between the molecular and electronic phase in electronic wavepackets in determining the excited state dynamics [1].

2.1 Spectroscopy of NO

Although ostensibly simple, diatomics display a variety of complexities in their Rydberg spectra due to the coupling between electronic and nuclear degrees of freedom; each rovibrational state of the ionic core has an associated set of Rydberg series resulting in a high density of states and congested spectra. In addition, Rydberg state interactions with valence states lead to dissociation and perturbations in line positions causing even greater complexity. Excitation *via* a specific rovibrational level of an intermediate restricts the number of accessible states and renders assignment more tractable whilst also allowing a degree of control over the final angular momentum of the Rydberg states accessed. This work involves the excitation scheme

$$\begin{aligned} &\mathrm{X}^2\Pi_{3/2}\,|v''=0, J''=3/2\rangle \\ &\qquad\xrightarrow{\omega_1} \mathrm{A}^2\Sigma^+\,|v', N'=0, J'=1/2\rangle \\ &\qquad\xrightarrow{\omega_2} \mathrm{NO}^+{}^1\Sigma^+\,|nlN^+\rangle\,. \end{aligned} \tag{2.1}$$

Here, n and l respectively denote the principal and orbital angular momentum quantum numbers of the Rydberg electron, and N^+ the rotational quantum number of the ionic core. v, N and J are the vibrational, rotational and total angular momentum quantum numbers with a single prime indicating an intermediate quantity and a double prime a ground state quantity. In order to analyse the experimental data, we must first establish a thorough understanding of the spectroscopy of each of the X, A and Rydberg states as well as the quantum mechanics that governs transitions between them. Of particular importance is the coupling between the various angular momentum constituents and this will be covered in the next section.

2.1.1 Hund's Cases

Hund's angular momentum coupling cases are idealised, limiting cases for diatomics and describe the influence that rotational and electronic motions have on one another.

There exist Hund's cases (a) to (e) but of most relevance to this work are cases (a), (b) and (d) and, as such, these are the only cases covered in this work[1]. The ground state of NO, $X^2\Pi_{3/2}$, is best described by case (a), the intermediate, $A^2\Sigma^+$, by case (b) and the Rydberg states by case (d). In the following, bold font indicates a vector quantity and italic font the quantum number associated with that physical quantity.

In Hund's case (a) it is assumed that the coupling between the electronic angular momentum (orbital, $\mathbf{L}$, and spin, $\mathbf{S}$) and the rotation of the nuclei is weak whereas the coupling of these with the internuclear axis is strong in comparison. As a consequence, $\mathbf{L}$ and $\mathbf{S}$ precess rapidly about the internuclear axis and, as such, are ill-defined. Their respective components along the internuclear axis, however, are well defined and combine to give the total angular momentum along the internuclear axis, $\mathbf{\Omega} = \mathbf{\Lambda} + \mathbf{\Sigma}$, where $\mathbf{\Lambda}$ and $\mathbf{\Sigma}$ are the projections of the electronic orbital and spin angular momenta respectively. $\mathbf{\Omega}$ then couples to the angular momentum of nuclear rotation, $\mathbf{N}$, to give the total angular momentum, $\mathbf{J} = \mathbf{\Omega} + \mathbf{N}$. The notation for a state described by Hund's case (a) is ${}^{2S+1}\Lambda_{\Omega}$.

Hund's case (b) corresponds to a situation in which the orbital angular momentum, $\mathbf{L}$, is still strongly coupled to the internuclear axis but the spin, $\mathbf{S}$, is now either uncoupled or very weakly coupled to the axis; $\mathbf{\Omega}$ is not defined and as such Hund's case (a) cannot be applied. In this case, $\mathbf{\Lambda}$ and $\mathbf{N}$ couple to form a resultant, $\mathbf{N}'$, which is the total angular momentum apart from spin. This then couples to the spin to give $\mathbf{J} = \mathbf{N}' + \mathbf{S}$. The notation for a state described by Hund's case (b) is ${}^{2S+1}\Lambda^p$ where p is the parity of the state.

Rydberg states are best described by Hund's case (d). In this case the Rydberg electron spends the majority of its time far away from the core and so can be treated independently from it. The angular momentum due to the core rotation, $\mathbf{N}^+$, thus couples with the orbital angular momentum of the electron, $\mathbf{l}$, to give the total angular momentum excluding spin, $\mathbf{N}' = \mathbf{l} + \mathbf{N}^+$. This then couples with the electron spin

[1]For a more complete description of Hund's cases see reference [73]

to give the total angular momentum $\mathbf{J} = \mathbf{N}' + \mathbf{s}$. The Rydberg series in this work are thus labelled by the notation $nl(N^+)$. Figure 2.1.1 gives the vector diagrams for Hund's cases (a), (b) and (d).

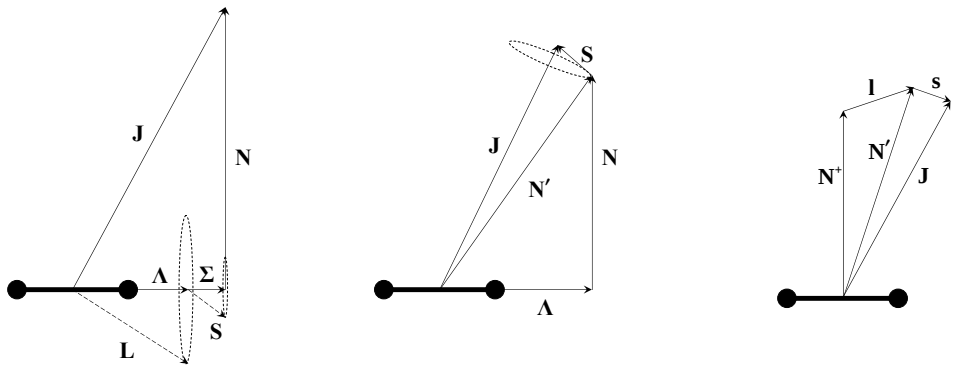

(a) Case (a) (b) Case (b) (c) Case (d)

Figure 2.1: Schematic illustration of the angular momentum coupling in NO. Hund's cases (a), (b) and (d) are shown by figures (a), (b) and (c) respectively.

2.1.2 Energies of the X, A and Rydberg States

The ground state of NO is described using a Hund's case (a) scheme. Since there is a single electron in a $2p\pi^*$ orbital it follows that $\Lambda = 1$ and $\Sigma = 1/2$. Therefore the ground state is split into two spin-orbit states; $X^2\Pi_{1/2}$ and $X^2\Pi_{3/2}$, and these are separated in energy by around 120 cm^{-1} [73]. In the following, a double primed quantity indicates a ground-state quantity and a single prime that of the intermediate. A superscript '+' indicates a quantity associated with the ionic core.

The energy of the rovibrational levels of the ground state can be calculated using [74]

$$E''_{vJ} = G''_v - D''_v + \frac{a''_v}{2} + B''_{vJ}(J'' + \frac{1}{2})^2 - D''_{vJ}(J'' + \frac{1}{2})^4, \tag{2.2}$$

where D''_v is the true rotational constant, a''_v is the energy separation between the two spin-orbit states, and B''_{vJ} and D''_{vJ} are effective rotational constants particular to each state. The energy zero is taken as the mid-point between the two electronic states and the subscript J indicates which of the spin-orbit states equation (2.2) is referring to; $J = 2(1)$ indicates an $F_1(F_2)$ state as will be discussed below. G''_v is the vibrational energy and is calculated using

$$G''_v = \omega''_e(v'' + \frac{1}{2}) - \omega_e x''_e(v'' + \frac{1}{2})^2 + \omega_e y''_e(v'' + \frac{1}{2})^3 - ..., \tag{2.3}$$

where ω''_e is the harmonic wavenumber and $\omega_e x''_e$ and $\omega_e y''_e$ are the first and second anharmonicity constants.

The A-state of NO is best described by a Hund's case (b) coupling scheme and the energies are calculated using [73]

$$E_{vN} = T'_e + G'_v + B'_v N'(N' + 1) - D'_v N'^2(N' + 1)^2, \tag{2.4}$$

where T'_e is the energy difference from the bottom of the A-state well to the bottom of the ground state well. The other constants have the same meaning as explained for equation (2.2) with the single prime indicating that we are referring to the intermediate state. In equation (2.4) the vibrational energy, G'_v, has exactly the same form as in (2.3) with the relevant quantities for the intermediate state substituted in. Spectroscopic quantities used to calculate the A and X energies are given in table (2.1) and are taken from references [73] and [75].

Each rotational level in the intermediate is split into two sub-levels according to $J' = N' + 1/2$ and $J' = N' - 1/2$; the former is denoted an F_1 state and the latter an

Table 2.1: Spectroscopic constants used in the assignment of the intermediate spectra. All numbers are given in cm^{-1} and were taken from references [73] and [75].

	$X^2\Pi_{3/2}$	$A^2\Sigma^+$
a_v	119.77	-
D_0	5.5x10^{-6}	-
B_{02}	1.72002	
D_{02}	9.8x10^{-6}	-
B_1	-	1.9678
D_1	-	5.4x10^{-6}
ω_e	1903.68	2374.31
$\omega_e x_e$	13.97	16.106
$\omega_e y_e$	-0.0012	-0.0465

F_2 state [58]. Similarly, the two spin-orbit levels of the X-state, $^2\Pi_{1/2}$ and $^2\Pi_{3/2}$, are labelled as F_1 and F_2 respectively. In the standard way, each transition $A^2\Sigma^+ \leftarrow X^2\Pi$ can be labelled using ΔJ_{fi} notation as one of a $P_{12}, P_{22}, Q_{12}, Q_{22}, R_{12}, R_{22}$ transition where the subscripts fi indicate the final and initial states in the transition and P, Q and R indicate $\Delta J = -1, 0$ and $+1$ respectively. Thus, the first transition in equation (2.1) is a P_{12} transition since this indicates a transition from the F_2 component of the $X^2\Pi$ state to the F_1 component of the $A^2\Sigma^+$ state and $\Delta J = -1$. The P_{12} branch was chosen since no other branches cross it and thus a particular rotational state of the intermediate may easily be selected. In chapter 4, we describe work in which we excite the Rydberg states *via* a vibrationally excited intermediate and observe interferences between competing dissociative and ionising decay channels, while in chapter 5 we draw a comparison between the spectroscopy and dynamics of Rydberg states converging to a vibrationless and vibrating core.

The energy of the Rydberg states is given by the well-known Rydberg formula

$$E_{\upsilon^+N^+nl} = I_{\upsilon^+N^+} - \frac{R_{\rm NO}}{(n-\mu_l)^2}, \tag{2.5}$$

as introduced in chapter 1. Here $I_{\upsilon^+N^+}$ is the ionisation potential for the core rovibrational state (υ^+N^+), $R_{\rm NO}$ is the Rydberg constant for NO equal to 109735.3 cm^{-1} , n is the principal quantum number and μ_l is the quantum defect.

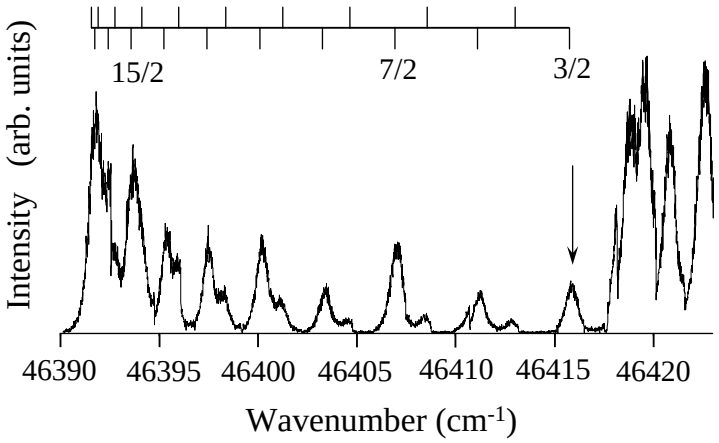

Figure 2.2: REMPI spectrum of the $\upsilon' = 1$, $\mathrm{P}_{12}(J'')$ branch of the A-state. J'' values are labelled with a comb and denote the rotational level of the ground state from which excitation takes place. The $\upsilon^+ = 1$ Rydberg states are accessed from the $|\upsilon' = 1, N' = 0, J' = 1/2\rangle$ state, indicated by an arrow.

2.1.3 The A to Rydberg Transition

In order to assign the experimental spectra it is necessary to understand which states may be populated from the intermediate. This can be accomplished through consideration of the appropriate selection rules and the conservation of angular momentum.

We define the total angular momentum of the A-state, the total angular momentum of the Rydberg state, and the angular momentum of the photon as $\mathbf{J'}$, $\mathbf{J}$ and $\boldsymbol{\gamma}$ respectively. It follows by conservation of angular momentum that the total angular momentum of the final Rydberg state must be the sum of the intermediate total angular momentum and the (unit) photon angular momentum. Hence

$$\mathbf{J} = \mathbf{J}' + \boldsymbol{\gamma} = \mathbf{J}' + \mathbf{1}. \tag{2.6}$$

The A-state angular momentum is a sum of rotational, $\mathbf{N}'$, and spin, $\mathbf{s}'$, angular momenta. Hence, using Hund's case (b) notation, we have

$$\mathbf{J}' = \mathbf{N}' + \mathbf{s}'. \tag{2.7}$$

Similarly, for the Rydberg state the total angular momentum is the sum of the orbital, $\mathbf{l}$, rotational, $\mathbf{N}^+$, and spin, $\mathbf{s}$, angular momenta. Using Hund's case (d) notation it follows that

$$\mathbf{J} = \mathbf{N}^+ + \mathbf{l} + \mathbf{s}. \tag{2.8}$$

Substitution into equation (2.6) yields

$$\mathbf{N}' + \mathbf{s}' + \mathbf{1} = \mathbf{N}^+ + \mathbf{l} + \mathbf{s}. \tag{2.9}$$

Since the spin of the outer electron is conserved we have $\mathbf{s}' = \mathbf{s}$. In addition, the Rotation-Spectator model [76, 77] states that the photon is absorbed by the excited electron as opposed to the core. The orbital angular momentum of the Rydberg electron then, is clearly just the sum of the intermediate orbital angular momentum and the unit photon angular momentum; $\mathbf{l} = \mathbf{l}' + \mathbf{1}$. Taking these conditions into account we arrive at

$$\mathbf{N}' = \mathbf{N}^+ + \mathbf{l}'. \tag{2.10}$$

That is, the final rotational states of the core that can be populated from our intermediate are determined by the vector sum of the intermediate rotational state and the

electronic orbital angular momentum. Additionally, parity must also be taken into consideration: for a non-zero transition moment we require the final and initial states involved in the transition (the Rydberg states and the intermediate, respectively) to have opposite parity. The parity of the intermediate is given by $p' = (-1)^{N'}$ and that of the Rydberg state by $p^+ = (-1)^{N^+ + l}$ by which the condition reduces to

$$p^+ p' = (-1)^{N^+ + l + N'} = -1. \tag{2.11}$$

Since in our case $N' = 0$ we arrive, trivially, at $N^+ + l =$ odd.

The A-state is labelled 3sσ but due to the non-Coulombic potential and non-spherical core it has mixed angular momentum character *i.e.* the angular part of the Rydberg wavefunction is now a superposition of spherical harmonics. The approximate composition of the A-state is 94% s character, 5% d character, 0.3% p character and smaller contributions from other angular momentum states [68, 78]. Since excitation is from the $N' = 0$ level, the strongest transitions expected are from the s-component to np(0) states with weaker contributions from the d-component to the np(2) and nf(2) series. In addition, weaker still transitions from the p-component to the ns(1) and nd(1) series are also possible.

2.2 The Quantum Defect

In order to assign the experimental spectrum according to equation (4.1) we require the case (d) quantum defects, μ_{lN^+}, for each of the Rydberg series accessible from the intermediate state. The case (d) defects are named thus since they are indicative of a Hund's case (d) type coupling in which the electronic motion is uncoupled to that of the core and the electron and core can be considered to be moving independently of one another - the electron is orbiting a vibrating and rotating core and its motion is not affected at a given moment by the rovibrational state of the ion. This is an appropriate way of describing Rydberg states since their radial wavefunctions are

strongly peaked at the outer periphery of their orbit and as such they encounter the core less frequently than a lower-lying state; at large radial distances (greater than a distance r_c, say) from the core they behave as though they are in a hydrogenic orbital seeing, on average, a single positive charge from the core. It is this behaviour that provides the similarity between equations (2.5) and (1.6). However, this description is only valid when the electron is far enough away from the core for the electronic and nuclear motions to be uncoupled. At smaller radial distances ($r < r_c$) the electron effectively reacts instantaneously to the motion of the nuclei and its angular momenta (spin and orbital) are thus strongly coupled to this motion. This corresponds to a case (b) coupling scheme and as such we require a solution to the Schrödinger equation that smoothly links between the two regions[2]. It is important to note that *all* states in a molecule penetrate the core region to some extent - it is through these short distance interactions that non-radiative decay mechanisms occur as discussed in the next section.

The short-range interactions are parameterised in terms of so-called eigen-channel quantum defects [11] and represent a phase shift of the electronic wavefunction in this region in a basis which diagonalises the short-range Hamiltonian. The procedure for obtaining the off-diagonal matrix elements of the Hamiltonian in a case (d) basis from the case (b) basis has been described by Vrakking [79] and involves a frame tranformation between the two. Here we are concerned only with the diagonal elements of this which yield the case (d) defects in terms of the eigen-channel defects, $\mu_{l\lambda}$, through [62]

[2]At distances $r > r_c$ the radial and angular parts of the Schrödinger equation are separable and the radial part reduces to the Coulomb equation which has has standard asymptotic solutions from which we recover the Rydberg formula (4.1). This separation of the space that the molecule inhabits into two physically distinct regions is fundamental to the theoretical treatment of Rydberg states using MQDT

$$\mu_{lN^+} = \sum_{\Lambda} \left[\langle N^+|\Lambda\rangle^{(Nl)} \right]^2 \mu_{l\lambda}, \tag{2.12}$$

where

$$\langle N^+|\Lambda\rangle^{(Nl)} = \langle N^+0|l-\Lambda, N\Lambda\rangle \, (2-\delta_{\Lambda 0})(-1)^{N+\Lambda-N^+} \tag{2.13}$$

and

$$\langle N^+0|l-\Lambda, N\Lambda\rangle = (-1)^{l-N}(2N^+ + 1) \times \begin{pmatrix} l & N & N^+ \\ -\Lambda & \Lambda & 0 \end{pmatrix}. \tag{2.14}$$

The matrix in (2.14) is a Wigner 3-j symbol and is given by [80]

$$\begin{aligned} \begin{pmatrix} l & N & N^+ \\ -\Lambda & \Lambda & 0 \end{pmatrix} =& (-1)^{l-N}(2N^+ + 1)^{-1/2} \Big[(2N^+ + 1) \frac{(s-2N^+)!(s-2N)!(s-2l)!}{(s+1)!} \\ & \times (l-\Lambda)!(l+\Lambda)!(N+\Lambda)!(N-\Lambda)!(N^+!)^2 \Big]^{1/2} \\ & \times \sum_{\nu} (-1)^{\nu} / [\nu!(l+N-N^+-\nu)!(l+\Lambda-\nu)!(N+\Lambda-\nu)! \\ & \times (N^+-N-\Lambda+\nu)!(N^+-l-\Lambda+\nu)!] \end{aligned} \tag{2.15}$$

where $s = l + N + N^+$ and the index ν takes all integral values for which the factorial arguments are non-negative. Table 2.2 gives the case (d) defects used in the assignment of our experimental spectra calculated from the eigen-channel defects of [62].

2.3 Decay Dynamics

As mentioned previously, Rydberg states are relatively long-lived with respect to radiative decay - their radial distribution functions are most intense at the outer periphery of the orbit and as such there is little overlap with lower-lying states;

l	$N^+ = 0$	$N^+ = 1$	$N^+ = 2$
0	-	0.210	-
1	0.703	-	0.697
2	-	-0.012	-
3	-	-	0.018

Table 2.2: The case (d) quantum defects used in the assignment of the experimental spectra.

consequently the probability of radiative decay is greatly reduced since the lifetime of a state $|nl\rangle$ is given by

$$\tau_{nl} = \Big[\sum_{n'l'} A_{n'l'nl}\Big]^{-1}$$

where $A_{n'l'nl}$ is the Einstein A coefficient which defines the spontaneous decay rate of the nl state to the lower-lying $n'l'$ state and $A_{n'l'nl} \propto |\langle n'l'|\, r\, |nl\rangle|^2$; this leads to an n^3 dependence of the lifetime [2]. Nevertheless, interactions between the Rydberg electron and the core can give rise to some rapid decay mechanisms, namely autoionisation and predissociation. Both of these processes can be seen as an exchange of energy between the nuclear and electronic degrees of freedom, facilitated by a collisional process and resulting in fragmentation of the molecule. These decay processes will now be considered in turn.

2.3.1 Autoionisation

The process of autoionisation can be seen as the following for the diatomic AB:

$$\mathrm{AB}(E^*) \xrightarrow{\text{electron}-\text{core interaction}} \mathrm{AB}^+(E^* - E_e) + e^-(E_e). \tag{2.16}$$

That is to say, the system is initially in a Rydberg state and proceeds, through some electron-core interaction, to an ion and an unbound electron. One way of

understanding this is as follows: the Rydberg electron is in a large orbit and spends the majority of its time at the outer turning point thus moving, on average, in the Coulomb potential due to a single charge. The electron accelerates back towards the core and collides with it inelastically. During this collision the core may relax (vibrationally, rotationally) and transfer this excess energy to the Rydberg electron; this may be enough to eject the electron from the molecule, thus forming an ion and an unbound electron. From a spectroscopic perspective, a Rydberg state is one that is bound with respect to direct ionisation but coupled to the continuum of a channel with a lower ionisation potential. The degeneracy between the discrete state and the continuum facilitates a non-zero probability of a transition between the two. In this event the electron is liberated from the attractive potential due to the core and gains kinetic energy equal to the difference in energy between the Rydberg state and the ionisation potential of the channel that it has autoionised into. The energy required for the autoionisation process can come from the rovibrational energy of the ionic core, this being particular to molecular systems of course, or from the spin-orbit interaction in the case of atoms.

2.3.2 Predissociation

As well as autoionising, molecules can predissociate. In this case the Rydberg electron collides with the core and as opposed to gaining energy from the core (as is the case with autoionisation) the electron transfers some of its energy to the nuclear degrees of freedom of the core; this energy may be enough to fragment the core into its atomic components. In general then, for a species AB that fragments to neutral products A and B, predissociation is the process

$$\mathrm{AB}(E^*) \xrightarrow{\text{electron}-\text{core interaction}} \mathrm{A}(E) + \mathrm{B}(E^* - E). \tag{2.17}$$

That is, the system is in an excited (Rydberg) state and through some electron-core

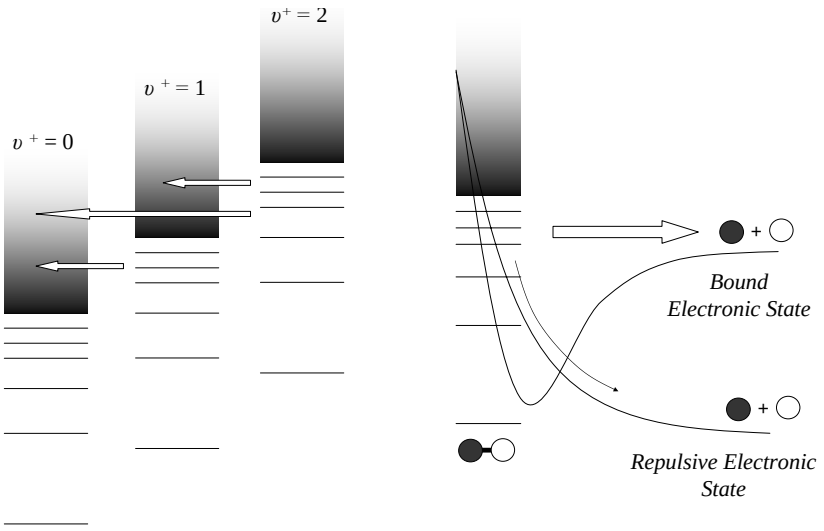

(a) Autoionisation (b) Predissociation

Figure 2.3: Schematic illustration of autoionisation and predissociation. Coupling between a Rydberg state and a continuum can result in a radiationless transition between the two resulting in the fragmentation of the molecule into ionic or neutral products.

interaction, the molecule breaks into neutral products. In this case, as in autoionisation, the orbiting Rydberg electron accellerates towards, and collides inelastically with, the core. The collision causes energy to be redistributed from the electronic to the nuclear degrees of freedom resulting in the fragmentation of the core into neutral products. Quantum mechanically, the bound Rydberg state is coupled to some dissociative continuum and the intersection of the two potential curves can result in the system crossing from the former to the latter, thus causing the molecule to dissociate; in other words, the degeneracy between the two allows for some probability amplitude of the Rydberg wavefunction to leak into the dissociative continuum. Note that for predissociation to occur this degeneracy need not be confined to a repulsive electronic state - if the Rydberg state lies above the dissociation limit of a bound electronic configuration then upon crossing the molecule vibrates/rotates to such an extent that the bond breaks yielding atomic products. Predissociation is illustrated

schematically in figure 2.3(b).

In the energy region considered in this work there are three open dissociation channels: N(^{4}S)+ O(^{3}P), N(^{4}S)+ O(^{1}D) and N(^{2}D)+O(^{3}P). The Rydberg states associated with the $^2\Pi$ configuration are perturbed strongly by the B$^2\Pi$ and L$^2\Pi$ valence states and MQDT has predicted that 90% of the np states decay *via* these states to N(^{2}D)+O(^{3}P) products [16, 65]. This assertion is supported by experimental studies [50] and it is this fast predissociation rate that accounts for the very broad lines observed for transitions to np states. The nf states are generally considered to be much less predissociative than the np states; the high orbital angular momentum character results in a high centrifugal barrier and consequently a weaker penetration of the core. However, the nf states are present in the fragment atom yield spectrum of Fujii and Morita and this is thought to be due to a supressed autoionisation rate [50]. Autoionisation and predissociation compete and the high centrifugal barrier increases the autoionisation lifetime such that states may still preferentially predissociate. Autoionisation is thought to be the dominant decay process in the ns Rydberg states [49] and although there is a weak interaction with the I$^2\Sigma^+$ valence state which converges to the N(^{2}D)+O(^{3}P) limit, the main dissociative pathway for this Rydberg series is *via* the A$'^2\Sigma^+$ state to N(^{4}S)+ O(^{3}P) products. In any case, in previous work [49] the np states are by far the most dominant feature of the N(^{2}D) yield spectrum and it is into this channel that we monitor decay in this work.

2.3.3 Fano Lineshapes

Autoionising resonances such as those discussed in section 2.3.1 were first discovered experimentally by Beutler and were conspicuous on account of their distinct asymmetric line profile. The asymmetric profile remained the source of some mystery until Fano constructed a theoretical description showing the lineshape to follow a simple formula given by [81]

$$R = \frac{(q+\epsilon)^2}{1+\epsilon^2}, \tag{2.18}$$

where q and ϵ are quantities defined in terms of the states involved in the autoionisation and the coupling between them as will be discussed shortly. Fano explained that autoionising resonances can be understood to be a consequence of the discrete state from one configuration interacting with the continuous states of another; that is, in terms of a *configuration interaction*. Although first explained in terms of autoionisation, predissociative resonances also display Fano lineshapes and as such may be characterised in the same way as autoionising ones through reference to equation (2.18).

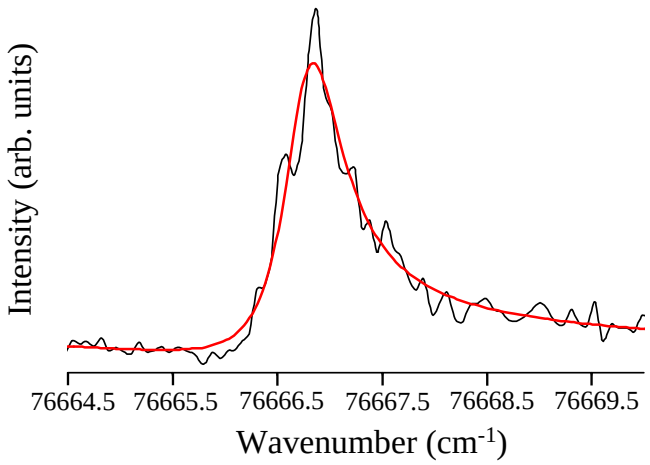

Figure 2.4: Experimental (grey trace) spectrum of the predissociating 21s(1) resonance. Overlaid (black trace) is the Fano profile derived by fitting equation (2.18) to the experimental data.

Fano lineshapes are evident throughout the spectra recorded in this work (see *e.g.* chapters 4 and 5); a typical example is given in figure 2.4 where equation (2.18) has been fitted to the experimental data. Although Fano resonances may be understood in terms of both scattering theory and configuration interaction, in this work we adopt the latter approach considering only the simple case of a single discrete state

interacting with a single continuum. While this is a great oversimplification of the multi-channel nature of a real system such as NO, it still yields information pertaining to the the many interacting Rydberg series present and an insight into the underlying dynamics of the excited states. To this end, the theoretical description of such a single discrete-single continuum interaction as outlined by Fano will be covered here.

Consider a number of zero-approximated states (*i.e.* a diagonal basis of the unperturbed Hamiltonian of the system) consisting of a single discrete state, $|\phi\rangle$, and a continuum of states, $|\psi_{E'}\rangle$. The perturbed system is thus defined by a matrix of elements according to

$$\langle\phi|H|\phi\rangle = E_\phi \tag{2.19a}$$

$$\langle\psi_{E'}|H|\phi\rangle = V_{E'} \tag{2.19b}$$

$$\langle\psi_{E''}|H|\psi_{E'}\rangle = E'\delta(E'' - E') \tag{2.19c}$$

where H is the total Hamiltonian and it is understood that E_ϕ lies within the continuous range of energies defined by the continuum, E'. $\delta(E'' - E')$ is the well-known Dirac delta function. The solution of such a system will have eigen-vectors of the form

$$\Psi_E = a\phi + \int b_{E'}\psi_{E'}\mathrm{d}E'; \tag{2.20}$$

that is, the full wavefunction is a superposition of the discrete state and the continuum with the quantities a and $b_{E'}$ determining the composition at a given energy, E[3]. Multiplication of the matrix (2.19) by the eigen-vector (2.20) in the usual manner

[3]It is implicit that both a and $b_{E'}$ are functions of E - for brevity this is not indicated unless necessary.

yields

$$aE_\phi + \int V^*_{E'} b_{E'} \mathrm{d}E' = Ea \tag{2.21a}$$

$$aV_{E'} + E' b_{E'} = E b_{E'}. \tag{2.21b}$$

Solving (2.21b) for $b_{E'}$ we have

$$b_{E'} = \frac{V_{E'} a}{E - E'}$$

which is divergent at $E = E'$. This is circumvented by the introduction of a formal solution of (2.21b) namely,

$$b_{E'} = \left[\frac{1}{E - E'} + z(E)\delta(E - E') \right] V_{E'} a. \tag{2.22}$$

This solution is due to Dirac with the understanding that integration of the function $z(E)$, which we take to be real, is only over the principal part and that the form of $z(E)$ will be determined by the details of the problem [82]. Substitution of (2.22) into equation (2.21a) gives

$$aE_\phi + P \int \frac{|V_{E'}|^2 a}{E - E'} \mathrm{d}E' + az(E)|V_E|^2 = Ea, \tag{2.23}$$

which, upon cancellation of a and rearrangement, yields

$$z(E) = \frac{E - E_\phi - F(E)}{|V_E|^2}. \tag{2.24}$$

Here, $F(E)$ is defined through

$$F(E) = P \int \frac{|V_{E'}|^2}{E - E'} \mathrm{d}E', \tag{2.25}$$

where P indicates the principal part of the integral.

Normalisation of the wavefunction (2.20) and subsequent determination of the coefficient a proceeds through evaluation of

$$\langle \Psi_{\bar{E}} | \Psi_E \rangle = a^*(\bar{E})a(E) + \int b^*_{E'}(\bar{E}) b_{E'}(E) \mathrm{d}E' = \delta(\bar{E} - E) \tag{2.26}$$

where $\bar{E}$ and E are energies within the range of interest. Substitution of (2.22) into (2.26) then yields

$$\begin{aligned} \langle \Psi_{\bar{E}} | \Psi_E \rangle = a^*(\bar{E}) \Big\{ 1 + P \int V^*_{E'} \mathrm{d}E' \Big[\frac{1}{\bar{E} - E'} + z(\bar{E}) \delta(\bar{E} - E') \Big] \\ \times \Big[\frac{1}{E - E'} + z(E) \delta(E - E') \Big] V_{E'} \Big\} a(E). \end{aligned} \tag{2.27}$$

Expansion of the squared brackets on the righthand side involves integration over a term $(\bar{E} - E')^{-1}(E - E')^{-1}$ which must be treated carefully since it is doubly singular at $E = \bar{E}$ (see appendix A of reference [81]); however, if this is worked through then the coefficient a is defined by

$$|a(E)|^2 = \frac{|V_E|^2}{(E - E_\phi - F(E))^2 + \pi^2 |V_E|^4}. \tag{2.28}$$

Defining the shift energy, $E_0 = E_\phi + F(E)$, and the half-width, $\Gamma/2 = \pi |V_E|^2$, gives

$$|a(E)|^2 = \frac{1}{\pi} \frac{\Gamma/2}{(E - E_0)^2 + (\Gamma/2)^2} \tag{2.29}$$

which then gives an insight into the effect of the continuum on the discrete state. The presence of the continuum, $\psi_{E'}$, dilutes the discrete state, ϕ, throughout a band of continuous states centered about the shifted energy at E_0. This dilution is Lorentzian in form as emphasised by the introduction of Γ and E_0 and the resulting form of equation (2.29). In particular, we note that if the system was prepared in the purely discrete state ϕ then it would autoionise with an average lifetime given by the uncertainty principle, $\hbar/2\pi|V_E|^2$.

In order to elucidate the asymmetric nature of Fano-profiles, consideration of the variation in transition probability from some initial state, $|i\rangle$, to the final state, $|\Psi_E\rangle$, must be made. That is, consideration of the quantity $|\langle \Psi_E | T | i \rangle|^2$ where T is some

suitable transition operator. To do this it is convenient to introduce a quantity, $\Delta = -\arctan(\pi/z(E))$, which both of the coefficients, a and $b_{E'}$, depend upon in the following manner[4]

$$a = \sin\Delta/\pi V_E \tag{2.30a}$$

$$b_{E'} = \frac{V_{E'}}{\pi V_E}\frac{\sin\Delta}{E-E'} - \frac{V_{E'}}{V_E}\cos\Delta\delta(E-E'). \tag{2.30b}$$

Consider then

$$\begin{aligned}\langle\Psi_E|T|i\rangle &= a\,\langle\phi|T|i\rangle + \int b_{E'}\,\langle\psi_{E'}|T|i\rangle \mathrm{d}E' \\ &= \frac{1}{\pi V_E}\Big[\,\langle\phi|T|i\rangle + P\int\frac{V_{E'}\,\langle\psi_{E'}|T|i\rangle}{E-E'}\mathrm{d}E'\Big]\sin\Delta - \cos\Delta\,\langle\psi_E|T|i\rangle \\ &= \frac{1}{\pi V_E}\,\langle\Phi|T|i\rangle\sin\Delta - \cos\Delta\,\langle\psi_E|T|i\rangle\end{aligned} \tag{2.31}$$

where we have introduced the shifted state

$$\Phi = \phi + P\int\frac{V_{E'}\psi_{E'}}{E-E'}\mathrm{d}E', \tag{2.32}$$

which is clearly the discrete state ϕ modified by some mixture of the continuum states. With (2.31) we have now arrived at the source of the asymmetry in an autoionising resonance. Examining the behaviour of Δ near the resonance at $E = E_0$, there is a sharp variation of $\sim\pi$ in moving through an energy of $\sim|V_E|^2$ about the resonance. This sharp variation in turn causes the matrix element $\langle\Psi_E|T|i\rangle$ to vary sharply; in particular, the two contributions from the transition to the modified state, Φ, and the continuum, $\psi_{E'}$, interfere with *opposite phase* on either side of the resonance. This is entirely by virtue of the coefficients of the two matrix elements on the right-hand

[4]The quantity Δ arises from the asymptotic behaviour of the states, $\psi_{E'}$, at large r, that being $\propto \sin[k(E')r+\delta]$. Superposition with (2.22) and subsequent integration yields a term $\sin[k(E)r+\delta+\Delta]$ and thus Δ is known as the *phase shift* due to the configuration interaction. The dependence of a and $b_{E'}$ upon Δ, (2.30), is easily verified through reference to (2.28) and (2.22).

side of (2.31). $\sin\Delta$ is an odd function of $E - E_0$ whereas $\cos\Delta$ is an even function of $E - E_0$ and the two contributions thus interefere constructively on one side of the resonance and destructively on the other. Not only this but the transition probablity falls to zero on one side of the resonance where

$$\tan\Delta = \pi V_E \frac{\langle\psi_E|T|i\rangle}{\langle\Phi|T|i\rangle}; \tag{2.33}$$

the point at which the transition probability falls to zero is sometimes referred to as the 'transmission window'.

The physically significant quantity that we wish to investigate is of course the transition probablility, $|\langle\Psi_E|T|i\rangle|^2$, but since there are two transistion pathways available (direct ionisation and ionisation *via* the mixed state) it would be more pertinent to investigate the quantity $R = |\langle\Psi_E|T|i\rangle|^2/|\langle\psi_{E'}|T|i\rangle|^2$; that is, the modulation of the continuum as a consequence of the discrete resonance imbedded within it. The most direct route to Fano's formula is as follows: we have

$$\begin{aligned} R = \frac{|\langle\Psi_E|T|i\rangle|^2}{|\langle\psi_{E'}|T|i\rangle|^2} &= \frac{|a\,\langle\phi|T|i\rangle + \int b_{E'}\,\langle\psi_{E'}|T|i\rangle \mathrm{d}E'|^2}{|\langle\psi_{E'}|T|i\rangle|^2} \\ &= \left|\frac{a}{\langle\psi_{E'}|T|i\rangle}\right|^2 |\langle\Phi|T|i\rangle + V_{E'} z(E')\,\langle\psi_{E'}|T|i\rangle|^2 \end{aligned} \tag{2.34}$$

where we have used the expression (2.22) and introduced the shifted state, $|\Phi\rangle$, defined by (2.32). Now, expressing $z(E')$ in terms of the half-width we have $z(E') = 2\pi(E' - E_0)/\Gamma$. Then, defining a dimensionless energy variable, ϵ, through

$$\epsilon = \frac{2(E' - E_0)}{\Gamma}, \tag{2.35}$$

and the shape parameter

$$q = \frac{1}{\pi V_{E'}} \frac{\langle\Phi|T|i\rangle}{\langle\psi_{E'}|T|i\rangle}, \tag{2.36}$$

while noting that

$$|a(E)|^2 = \frac{1}{\pi^2 |V_E|^2} \frac{1}{1+\epsilon^2}, \tag{2.37}$$

by subsitution into (2.34) we find

$$\begin{aligned} R &= \frac{1}{\pi^2 |V_{E'}|^2} \frac{1}{\epsilon^2 + 1} |\pi V_{E'} q + \pi V_{E'} \epsilon|^2 \\ &= \frac{(q+\epsilon)^2}{1+\epsilon^2} \end{aligned} \tag{2.38}$$

which is the well known Fano formula. It is important at this juncture to indicate the physical meaning of the quantities in (2.38). The reduced energy, ϵ, is proportional to the quantity $E - E_0 = E - E_\phi - F(E)$ and thus centres the resonance at the *shifted* resonance position; as we scan through the energy we determine the shifted resonance, E_0, not the unperturbed resonance position, E_ϕ. Correspondingly, an experimental investigation allows us to divulge information pertaining to a transition to the resonance as modified by the presence of the continuum, $\langle \Phi | T | i \rangle$, not to the unperturbed state itself, $\langle \phi | T | i \rangle$. In addition, $\Gamma \propto |V_E|^2$ and hence the linewidth gives a direct indication of the degree of coupling between the discrete state ϕ and the continuum in which it is imbedded, $\psi_{E'}$; a broad peak is indicative of a strong coupling between the two. The quantity, q, is the *shape index* and is a constant for a given resonance. If $q = 0$ then we have a so-called window resonance and if $q \to \pm\infty$ then the resonance has a totally symmetric Lorentzian lineshape. The sign of q determines whether the transmission window occurs to either high or low energy of the resonance [12]. Figure 2.5 gives some examples of (2.18) plotted against the reduced energy for various values of the shape index, q.

Equation (2.18) is derived for the case of a single, well isolated resonance interacting with a single continuum in an atomic system. It is equally applicable to molecular systems however where, instead of a degeneracy between a Rydberg state and an ionisation continuum of an excited electronic state, we may have degeneracy with either an ionisation limit of some rovibrational state of the core, or else the continuum as-

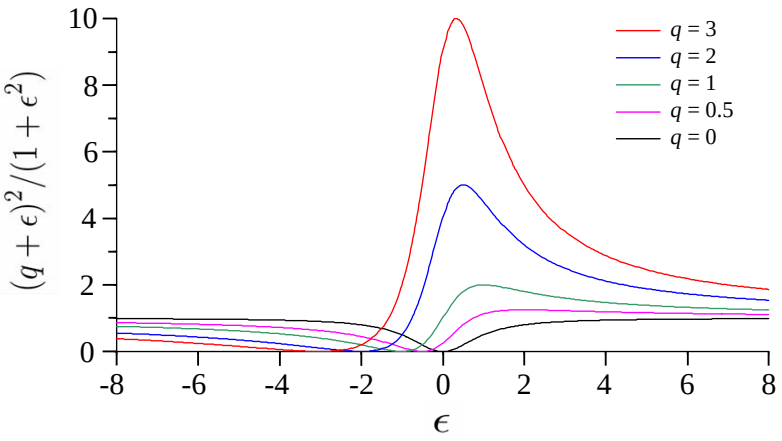

Figure 2.5: Plots of equation (2.18) against the reduced energy. For negative values of q, reflect the cuve about $\epsilon = 0$

sociated with a bound or repulsive electronic state of the molecule. The first of these two leads to molecular autoionisation and the second to predissociation. Thus the theory outlined by Fano holds equally well for either of the decay processes outlined in section 2.3.

2.4 Summary

This chapter has outlined previous work that has concentrated on nitric oxide and covered the motivation for using NO in the current work. In addition, the spectroscopy pertinent to the investigation of its energetic structure has been detailed including the calculation of energy levels relevant in this investigation. Through consideration of Hund's cases, selection and propensity rules, as well as the calculation of quantum defects, the method used in the assignment of the experimental spectra has been related. Finally, the theory that describes a single discrete state interacting with a single continuum has been covered and the derivation of the Fano lineshape formula appropriate to the resonances encountered here shown. The physical origins of the shape parameter, q, and the linewidth, Γ, have been discussed giving an indication

their implications for the current study.

Chapter 3

Experimental

In the work presented in this thesis Rydberg states converging to the $v^+ = 1$ and $v^+ = 0$ ionisation limits of the NO^+ core are investigated. The experimental set-ups for both sets of experiments in this work are essentially the same and as such the experimental details for both chapters are included below and a note made of any differences.

3.1 Laser System

A schematic of the excitation scheme used is given in figure 3.1 and a schematic of the optical layout is given in figure 3.2. A 20 Hz Q-switched Nd:YAG laser (Continuum: Powerlite) produces 10 ns long pulses of light at 1064 nm; this output is frequency doubled to generate 532 nm pulses of light with energies of approximately 400 mJ/pulse and bandwidth near 0.05 cm^{-1} which are used to pump two dye lasers. 40% of the output pumps the first dye laser (Continuum: ND6000); for the $v^+ = 1$ experiments the laser was operated with DCM[1] dye in methanol to produce output in the range 616-678 nm. For the $v^+ = 0$ work the dye used was Pyridine 1[2] dissolved in

[1] [2-[2-[4-(dimethylamino)phenyl]ethenyl]-6-methyl-4H-pyran-4-ylidene]-propanedinitrile.

[2] [2-[4-[4-(dimethylamino)phenyl]-1,3-butadienyl]-1-ethylpyridinium monoperchlorate.

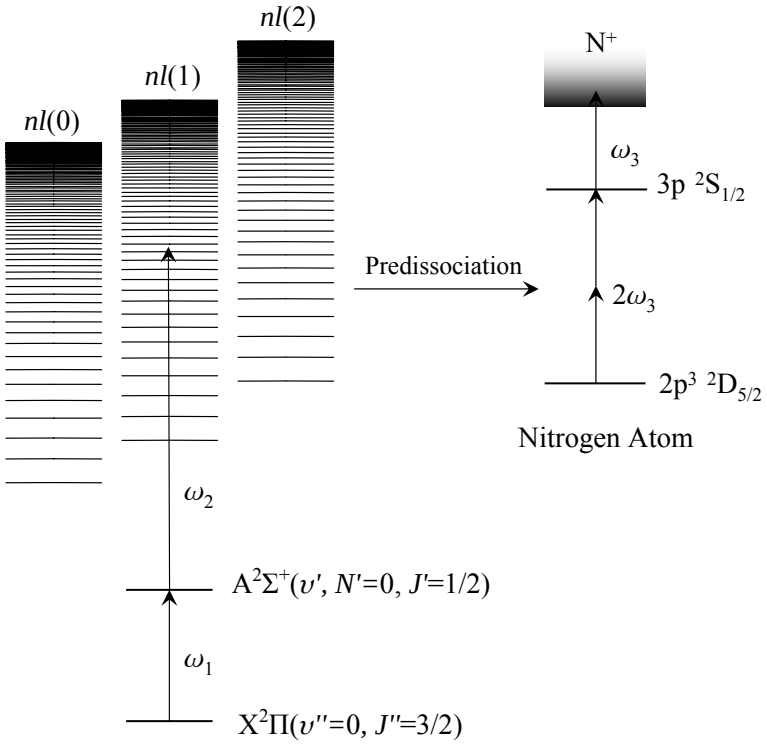

Figure 3.1: Schematic of the excitation scheme used in this work. A single photon, ω_1, accesses the rotationless $\upsilon' = 0$ or $\upsilon' = 1$ level of the $A^2\Sigma^+$ state. A second photon, ω_2, then scans through the Rydberg levels which may autoionise or predissociate. The dominant decay channel in the predissociation process is to $N(^2D) + O(^3P)$ atomic products *via* the $B^2\Pi$ valence state and decay into this channel is monitored by (2+1) REMPI of the nitrogen atom; a third photon, ω_3, is in two-photon resonance with the $3p\ ^2S_{1/2} \leftarrow 3p^3\ ^2D_{5/2}$ transition and a third ionises the atom which is then detected.

ethanol producing output in the range 645-730 nm. In both cases the dye laser output is frequency tripled using a potassium dihydrogen phosphate (KDP) crystal followed by a β-barium borate (BBO) crystal to produce UV light near 215 nm or 226 nm for the $\upsilon^+ = 1$ and $\upsilon^+ = 0$ experiments, respectively. This process is not 100% efficient and the waste light is separated using a Pellin-Broca prism and discarded to leave the UV. This photon, ω_1, is used to access a specific rovibrational state of the intermedi-

ate in the $A^2\Sigma^+ |v'N'J'\rangle \overset{\omega_1}{\leftarrow} X^2\Pi_{3/2} |v'' = 0, J'' = 3/2\rangle$ transition. A half waveplate is positioned in between the KDP and BBO crystals (see figure 3.2) in order to control the intensity of the light produced from the mixing process. Rotating the waveplate rotates the polarisation of the light's electric field thus modifying the efficiency of the mixing process in the BBO crystal and ensuring that the intensity of the tripled light isn't high enough to cause REMPI of the intermediate state. The remaining 60% of the second harmonic output of the Nd:YAG laser pumps a second dye laser (Sirah: Cobra) operating with DCM dye in DMSO (dimethyl sulfoxide). This produces light of wavelength in the range 626-685 nm which is frequency doubled using a KDP crystal to produce pulses of ∼10 mJ near 313-343 nm. The KDP crystal is housed inside a computer controlled auto-tracking system attached to the Sirah and a calibration is carried out prior to the experiment so that the power of the laser is kept constant as the wavelength is scanned. This photon, ω_2, accesses the Rydberg states in the $NO^+ |nlN^+\rangle \overset{\omega_2}{\leftarrow} A^2\Sigma^+ |v'N'J'\rangle$ transition.

In order to investigate the decay characteristics of the Rydberg states we require a method of collecting the products from the autoionisation and predissociation processes. This is done through application of a pulsed electric field that accelerates positively charged ions to a detector where the ion flux registers as a current. In the case of autoionisation the product is ionic and can thus be detected directly. The products from predissociation are neutral and consequently a second excitation scheme is employed to ionise the nitrogen fragment prior to detection. A second Nd:YAG (Continuum: Precision II) generates 10 ns long pulses of light of wavelength 532 nm at around 550 mJ/pulse and a bandwidth of approximately 0.05 cm^{-1} . 40% of the laser power pumps a third dye laser (Continuum: ND6000) operating with fluoroscein 548[3] in methanol generating 220 mJ light at 544 nm. This is frequency mixed with 10% of the residual 532 nm Nd:YAG output in a BBO crystal producing 40 mJ light at 269 nm which is used in a REMPI procedure that ionises the nitrogen atom.

[3] 2',7'-dichloro-3',6'-dihydroxy-spiro[isobenzofuran-1(3H),9'-[9H]xanthen]-3-one

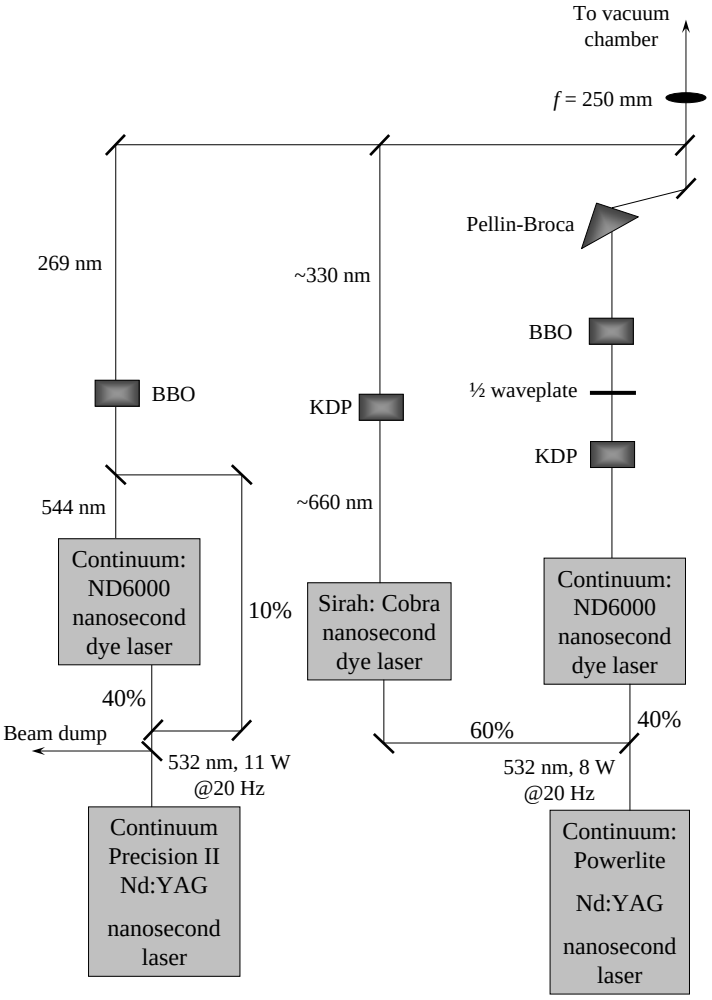

Figure 3.2: Schematic of the optical layout used.

Predissociation of the np states leads to a fragment nitrogen atom in the $2p^3\ ^2D_J$ state. This state has two spin-orbit states corresponding to $J = 5/2$ and $3/2$. The former is expected to be populated more due to its higher multiplicity and as such we probe this component by employing a three-photon (2+1) REMPI at 269 nm. Thus, a third frequency, ω_3, corresponding to a wavelength of 269 nm, is in two-photon resonance with $3p\ ^2S_{1/2} \leftarrow 3p^3\ ^2D_{5/2}$ transition and a third photon ionises the atom. In order to obtain the correct wavelength for the REMPI process the first two lasers are blocked while the wavelength and angle of the BBO crystal are altered. An accidental

resonance causes some predissociation which appears as a REMPI signal on the oscilloscope once the wavelength required for the REMPI process has been selected. The laser pulses are combined using a set of dichroic mirrors and focussed ($f = 250$ mm) into the vacuum chamber. A fraction of the laser light from the Sirah is coupled *via* a fibre optic to a wavemeter which measures and records the wavelength every five laser shots and is synchronised with the data aquisition software.

3.2 Vacuum Apparatus

The vacuum chamber consists of three regions: the source, interaction, and detection regions. The source region is pumped by a 700 $l\text{s}^{-1}$ diffusion pump (BOC:Edwards) backed by a rotary pump. A butterfly valve separates the diffusion pump from the chamber. The source region houses the gas nozzle and is held at a pressure of $\sim 10^{-7}$ mbar, rising to $\sim 10^{-5}$ mbar when the gas nozzle is in operation. The amount of gas entering the chamber is controlled by the pulse duration of the gas nozzle; this is around 200 µs at a backing pressure of around 2 bar. The interaction region is separated from the source region by a beam skimmer which extracts the centre line of the beam resulting in an improved signal to noise ratio. The laser light enters the chamber through a Brewster window into the interaction region where it crosses the molecular beam between a pair of capacitor plates. After the ionic products have been formed, a pulsed electric field is applied across the plates and accelerates the ions down a 250 mm field-free time-of-flight tube to detection chamber housing a microchannel plate (MCP) detector. The MCP (Hamamatsu: F4655-10) consists of two highly resistive plates with a dense series of channels drilled into them, each about 10 µm in diameter - hence 'microchannel'. These channels are drilled at an angle to the surface and the two plates rotated 180° to one another so that the channels make a chevron shape. The angle of the channels ensure that upon arriving at the detector a charged particle is guaranteed to collide with the wall of the MCP. The

impact of the collision causes a cascade of electrons which subsequently collide with the walls ejecting more electrons in a chain reaction of collisions. These electrons exit the channel and are detected as a current at an anode.

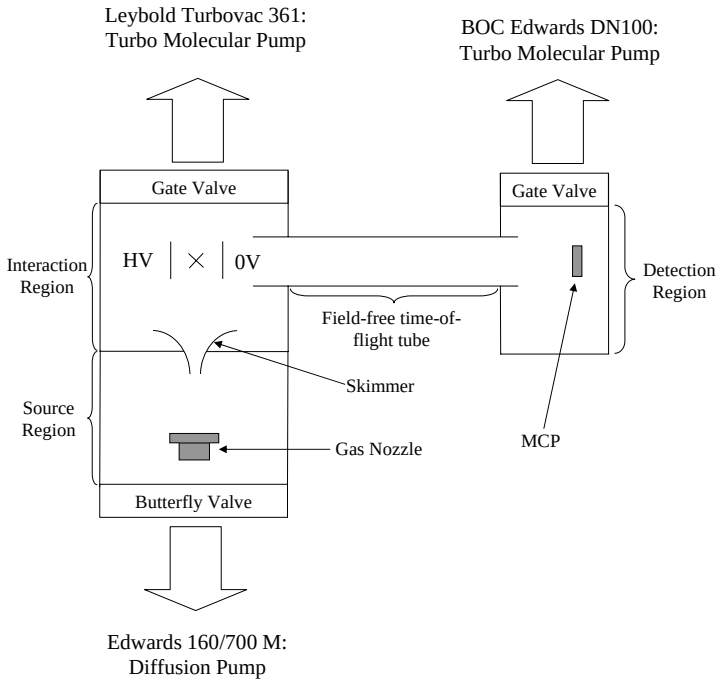

Figure 3.3: Illustration of the vacuum apparatus. The laser light arrives into the interaction region at the position marked by the cross, perpendicular to the page.

The pulsed electric field strength is set to 2 kV/cm for the predissociation experiments but only 50 V/cm for the autoionisation experiments. The reasoning behind this is two-fold: firstly, the detection efficiencies for the two decay processes are widely different. In the case of the autoionisation experiments, the pathway to the NO^+ product involves two photons followed by autoionisation from the Rydberg states. In contrast, the route to the N^+ ion involves two photons to access the Rydberg states followed by predissociation and finally a three photon REMPI process. Consequently the predissociative signal is much reduced relative to the autoionisation process; the increased amplitude of the pulsed field improves this signal considerably. The second

reason for the difference in extraction field is that Rydberg states are field ionised at relatively low applied fields. The field must therefore be kept below the field ionisation threshold to ensure that NO^+ ions produced solely from autoionisation are collected and not those from pulsed field ionisation of the residual Rydberg state population. Note that because of the different pulsed fields used in the autoionisation and predissociation experiments it is necessary to gate the appropriate signal on the oscilloscope and carry out separate runs of the experiment for either decay process.

The interaction region is pumped by a turbo molecular pump (Leybold: Turbovac-361) backed by a rotary pump and is held at a pressure of 10^{-8} mbar rising to 10^{-7} mbar when the gas nozzle is in operation. The MCP must be operated at high vacuum and this is achieved by way of a second turbo molecular pump (Edwards: EXT-250) backed by the same rotary as the other turbo molecular pump. This holds the pressure in the detection region to around 10^{-8} mbar at all times. Both turbo molecular pumps are separated from the chamber by gate valves as indicated in figure 3.3.

3.3 Timing

The relative time of arrivals of the gas pulse, the intermediate and Rydberg laser pulses, the REMPI pulse in the case of the predissociation experiments, and the pulsed electric field are controlled by a set of commercial delay generators. Figure 3.4 is a block diagram illustrating the relevant connections and delays. Initially a pulse generator (Thandar TG105) generates two transistor-transistor logic (TTL) pulses which act as the master trigger for the experiment. The first of these triggers the gas nozzle. After a delay of around 5 ms the second pulse triggers a delay generator (DG535-1 in figure 3.4) which produces three TTL pulses each with independent delays. Two pulses of 10 µs duration trigger the flash lamps (99 µs delay) and Q-switch (280 µs delay) of an Nd:YAG laser (Nd:YAG-1 in figure 3.4). The third pulse

triggers a second delay generator (DG535-2 in figure 3.4) which triggers the digital oscilloscope and pulsed electric field after delays of 295 µs and 325 µs respectively. For the predissociation experiments an extra delay generator (DG535-3 in figure 3.4) is employed and triggered from the first delay generator; after a delay of around 20 µs the flashlamps of a second Nd:YAG (Nd:YAG-2 in figure 3.4) are triggered followed by the Q-switch around 255 µs after. The relative time of arrival of these elements into the interaction region must be precise in order for the experiment to work and all are regularly optimised to generate the maximum signal. We found that the optimum signal was acquired when the first two lasers arrived at the same time and, in the case of the predissociation experiments, the third around 10 ns after this. The pulsed extraction field is applied around 100 ns after the final pulse; this delay ensures that all relevant decay processes have occurred by the time the extraction pulse is applied and also that the experiment takes place in a field free environment.

3.4 Data Acquisition

Ion flux at the MCP causes a current which is fed through a fast pre-amplifier (< 1 ns) to a digital oscilloscope. The current provides a measure of the number of ions incident at the detector and by plotting the measured intensity as a function of wavelength we can build a spectrum. In the predissociation experiments there are two distinct signals, one for the NO^+ ions and one for the N^+ ions. These are distinguishable by their time of flight, t, given by

$$t = d\Big(\frac{m}{2QV}\Big)^{1/2}. \tag{3.1}$$

Here, m and Q are the mass and charge of the ion, respectively, d is the distance to the detector and V is the accelerating voltage. Since the mass of NO^+ is greater than that of the nitrogen ion any signal due to the latter will occur before that of the former; by separating the various products by their differing time-of-flight we

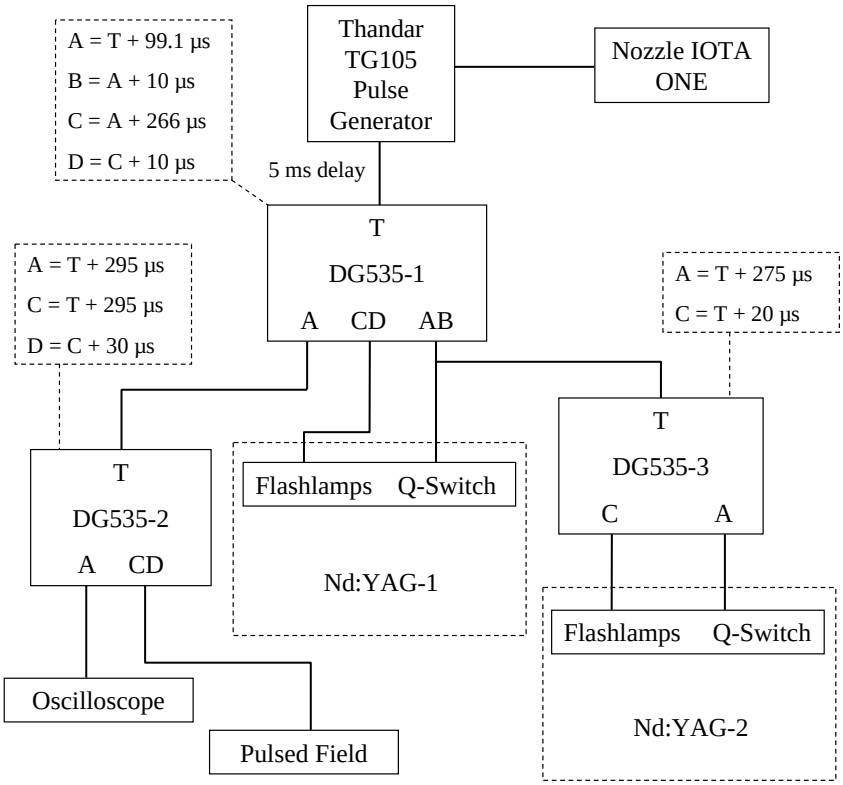

Figure 3.4: Block diagram showing the various components, connections and timings used to control the equipment used in the experiments.

selectively measure the signal due to predissociation or autoionisation.

In order to record a spectrum, the appropriate signal is gated on the oscilloscope (a typical signal covers about 10-20 ns), the wavelength is scanned through and the signal intensity from the MCP integrated and recorded as a function of the wavelength. To do this, a Labview programme triggers the Sirah laser and synchronises the wavelength readings with the wavemeter and oscilloscope reading. The Labview programme receives three pieces of information before beginning the scan: the start wavelength, the end wavelength, and the wavelength increment. The Sirah then initialises and moves to the start wavelength. Once the scan is started, the data collection is triggered on the Labview programme. This integrates the waveform on the oscilloscope and averages it over 20 shots to provide one intensity measurement at a given wavelength.

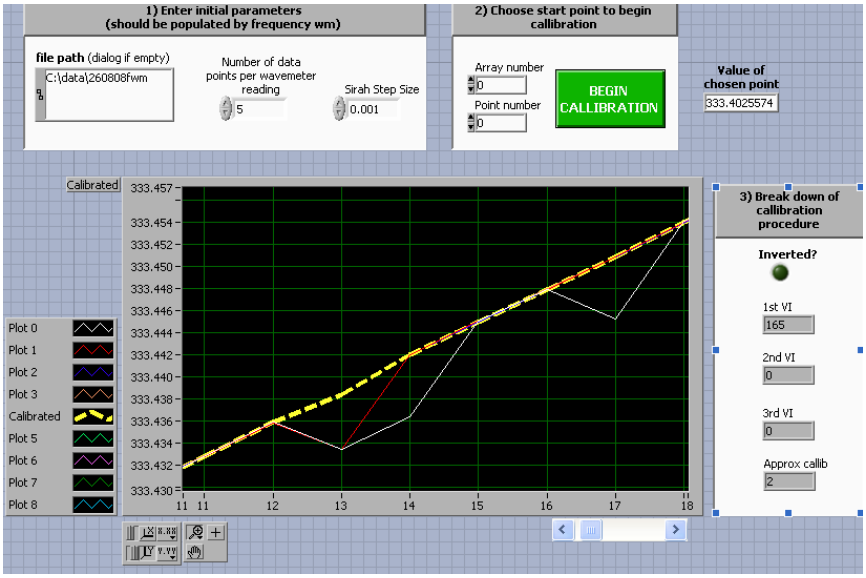

Figure 3.5: Screen dump of the Labview calibration subprogram. The solid coloured lines indicate wavemeter readings and the dashed yellow line the calibration line.

Every fifth intensity measurement the wavemeter measures the wavelength four times and records it to a file. If the measured wavelength lies far from that expected then the measurement is repeated until it lies within a specified error range. Once this condition is satisfied the Sirah moves through one increment and the process is repeated. When the scan has finished, a calibration subprogramme is initiated and reads the laser increment, wavelength measurements, number of intensity readings per measurement, and number of wavelength readings at each measurement step.

Figure 3.5 is a screen dump of the calibration subprogram. Labview displays the wavemeter readings as a graph and the solid coloured lines correspond to these readings. There is a systematic error in the wavemeter that leads to parallel calibration lines such as those shown in figure 3.5. A comparison between the two lines and known calibrated spectra indicates that the upper line is correct and thus the wavemeter is prone to wavelength measurements slightly lower than the actual value. Since this discrepancy is only 0.006 nm away from the true value it is not automatically discarded by the programme. To calculate a calibration line, the user picks a cell number

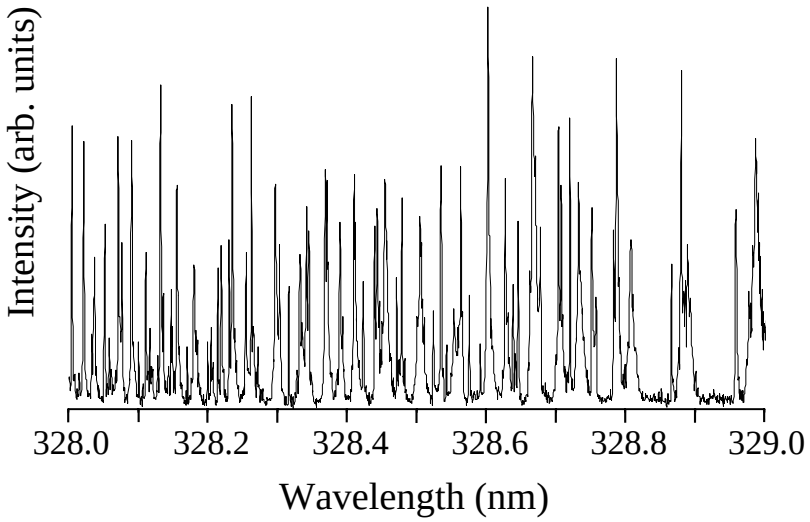

Figure 3.6: Example of combined intensity measurements and calibrated wavelengths to form a spectrum.

and the appropriate array and the calibration moves along this line taking an average of data lying within 0.0005 nm. The program then inserts a spline joining the data points to form the calibration line and this is the bold yellow line in figure 3.5. This calibration line can be easily checked throughout the wavelength range in order to gain an idea of the accuracy of the calibration process. The intensity profile and the splined calibrated wavelength measurements are then combined to produce the final spectrum (see, for example, figure 3.6).

Chapter 4

Interferences between competing ionisation and dissociation decay pathways in NO

The dynamics of super-excited Rydberg states (that is, states lying above the first ionisation limit) are of interest not only as model systems for the investigation of non-radiative decay pathways in larger molecules, but also as prototypes for coherent control. Such dynamics are generally complicated as a result of the many open decay channels available. In particular it is the competition between these channels that complicates the dynamics and hinders analysis; any attempt to drive the formation of one chemical product above all others, such as those made in the field of coherent control [18], therefore, are underpinned by the interplay between the various decay mechanisms available in the excited state. Thus, a thorough understanding of non-radiative decay processes and the interferences that occur between competing decay channels has broad significance for coherent control in molecular systems and in particular for the design and implementation of intuitive control schemes.

A great many experimental and theoretical studies have taken place concerning control between different decay pathways, and with varying success. Among the first

were the frequency domain experiments in which control is accomplished through the manipulation of interferences between different excitation pathways, as pioneered by Brumer and Shapiro [83,84]. This approach takes advantage of the energy dependent phase difference (or phase lag) between two excitation pathways and is most prominent near the quasi-bound states imbedded in the continua where the wavefunction contains components from the discrete states as well as from competing ionisation and dissociation continua. The duality of the wavefunction is manifest in the phase lag which therefore provides phase sensitive information regarding the discrete and continuum states as well as an insight into the control mechanism. Unfortunately, the level of control achieved experimentally is often disappointing and short of that predicted theoretically [21]. Conversely, other attempts involving the use of iterative algorithms to optimise the phase and amplitude of the frequency components of broad bandwidth laser pulses [85–87] have met with success, even in large molecules, but the complex form of the wave generated obscures the underlying physics and it is often difficult to obtain a complete understanding of the processes that drive the control mechanism. Perhaps due to the experimental and theoretical difficulties associated with such studies, there have been relatively few detailed investigations of the quantum mechanical interferences between the non-radiative decay channels which form the basis for these coherent control schemes [88,89].

Given the difficulty in fully elucidating the dynamics that drive control schemes in large molecular systems, it is instructive to turn to simpler systems in which the interfering decay pathways can be fully identified in order to construct an intuitive control scheme that is completely understood. As outlined in chapter 1, NO is an ideal test bed in which to realise such experiments and previous work in our group has already exploited the interplay between electronic and molecular phase to control the ionisation:dissociation ratio in the time domain [38]. While impressive as a study in itself, it is difficult to fully unravel the relationship between the phase and the ratio of ionisation to dissociation without quantitative knowledge of all of the other decay

routes available in the excited state. To this end, here we present a detailed investigation of super excited Rydberg states of NO in the energy range where dissociation and ionisation compete; namely, above the first ionisation threshold. Fano parameters and lifetimes are determined giving an indication of the relative coupling between members of the dominant np(0) and nf(2) series and the continuum, and we show how variations in the non-adiabatic coupling between the electronic and vibrational degrees of freedom manifest themselves as constructive and destructive interferences in the ionisation and dissociation channels.

4.1 Experimental

The experimental set-up used in this work has been described in detail in chapter 3 and as such only the details are covered here. The excitation and probing schemes used in the experiment are shown in figure 4.1. We have employed a $(1 + 1')$ double resonance excitation scheme to access Rydberg states converging to the $v^+ = 1$ ionisation limit of the ion core *via* the $A^2\Sigma^+(3s\sigma)$ intermediate state. The use of an intermediate state eliminates band congestion as discussed in section 2. A single photon, ω_1, corresponding to a wavelength of around 215 nm pumps the $A^2\Sigma^+ |v' = 1, N' = 0, J' = 1/2\rangle \leftarrow X^2\Pi_{3/2} |v'' = 0, J'' = 3/2\rangle$ transition and a second photon, ω_2, corresponding to a wavelength of around 330 nm scans through the Rydberg states above the first ionisation threshold where there is competition between autoionisation and predissociation. Vibrational transitions are controlled by the Franck-Condon principle which allows mainly $\Delta v = 0$ transitions due to the similarity between the potential curves of the Rydberg states and the A-state. In this energy region there are three open dissociation channels but it has been predicted by theory [65] and verified by experiment [50] that the Rydberg states in this energy region mainly dissociate *via* the $B^2\Pi$ and/or $L^2\Pi$ valence states to $N(^2D) + O(^3P)$ products (see section 2.3.2). In this work we probe decay into this dominant dissocia-

tion channel through a (2+1) REMPI process using a third photon, ω_3, corresponding to a wavelength of wavelength 269 nm that photoionises the N(^{2}D) product in a three photon process enhanced by two-photon resonance with the 3p $^2S_{1/2} \leftarrow 2p^3\ ^2D_{5/2}$ transition. ω_1 and ω_2 arrive simultaneously while there is a time delay of approximately 10 ns before the arrival of the third pulse. The ionic products of either decay mechanism are accelerated down a 250 mm time-of-flight tube by a pulsed electric field (Predissociation experiment: 2 kV, autoionisation experiment: 50 V in order to avoid field ionisation of the Rydberg population. The field is applied around 100 ns after the arrival of the first pulse) towards an MCP where they are detected. The two ion signals are distinguished by their time-of-flight.

The powers of each of the lasers must be delicately balanced in order to record accurate spectra of both the ionising and dissociating processes. In order to avoid REMPI of the intermediate state the power out of the first dye laser (red light) is kept to approximately 15 mJ per pulse and then cut down further by the mixing process and a half-wave plate. In addition, the energy of the second laser is suitable for a (2+1) REMPI from the ground state *via* the $E^2\Sigma^+$ state [90,91] and as such the power is kept to around 10 mJ per pulse to avoid reflecting the band structure of the E state in the autoionisation spectra.

4.2 Results and Discussion

Figure 4.2 shows experimental spectra taken in the total energy range 76550-76900 cm^{-1}. Frequency combs indicate the unperturbed positions of the dominant Rydberg series calculated using

$$E_{v^+N^+nl} = I_{v^+N^+} - \frac{R_{\mathrm{NO}}}{(n-\mu_l)^2}, \tag{4.1}$$

where $E_{v^+N^+nl}, I_{v^+N^+}, R_{\mathrm{NO}}$ and μ_l are the energy, ionisation potential, Rydberg con-

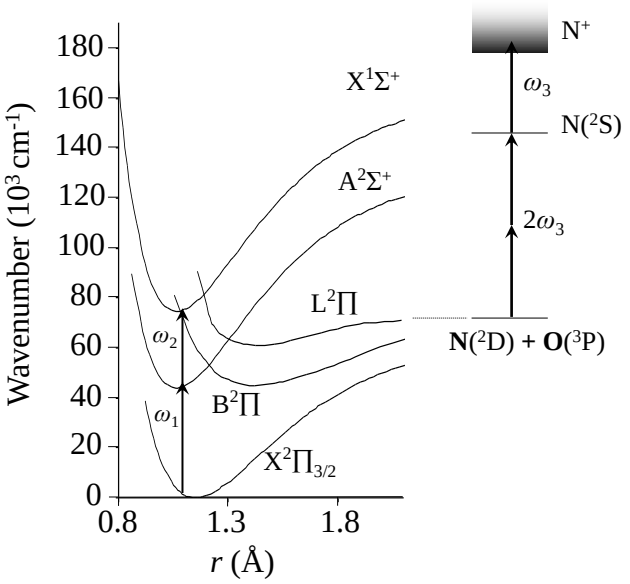

Figure 4.1: Illustration of the excitation scheme used in this work. A single photon (ω_1) pumps the $A^2\Sigma^+ \leftarrow X^2\Pi_{3/2}$ transition and a second (ω_2) scans through the Rydberg levels which may autoionise or predissociate. The dominant decay channel in the predissociation process is *via* the $B^2\Pi$ state to $N(^2D)$ and $O(^3P)$ neutral products. This is probed by (2+1) REMPI of the nitrogen fragment *via* the $N(^2S)$ state which is then detected.

stant and quantum defect as defined in section 1.1. For clarity, selected regions of the spectrum have been expanded and are shown in figures 4.3, 4.4 and 4.5. The ionisation spectrum (upper trace) exhibits sharp, well-defined peaks of similar intensity and linewidth, and is dominated by the np(0) and nf(2) series with weaker contributions from the ns(1), nd(1) and np(2) series. This behaviour persists to around 76775 cm^{-1} where there is a general broadening of the peaks and a rise in the baseline towards 76900 cm^{-1} . The appearance of the dissociation spectrum (lower trace) is in stark contrast: at low energy, from around 76550 cm^{-1} to 76650 cm^{-1} , there are intense, broad features attributable to the ns(1), nd(1) and np(2) series as well as the np(0) and nf(2) series (see figure 4.3). While hardly present at all in the ionisation spectra, the ns(1) lines are as intense as the np(0) and nf(2) resonances in the

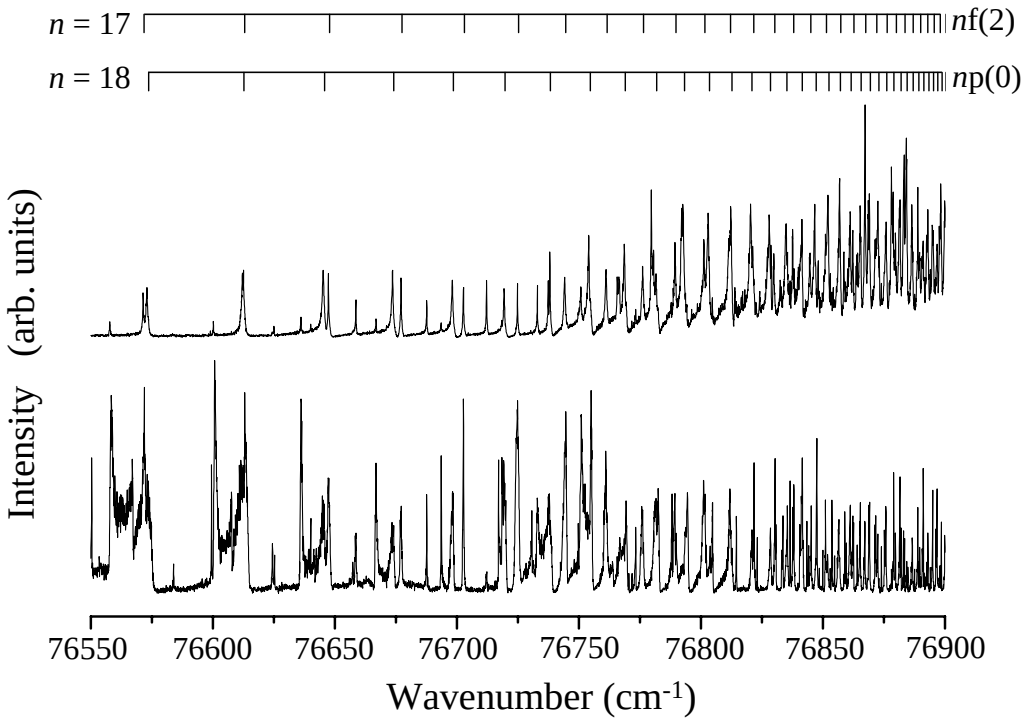

Figure 4.2: Autoionising (upper trace) and predissociating (lower trace) spectrum of Rydberg states populated *via* the $A^2\Sigma^+ |v' = 1, N' = 0, J' = 1/2\rangle$ state. The dominant np(0) and nf(2) series are labelled by frequency combs that mark the unperturbed line positions as calculated from (4.1). The energy is referenced to the $X^2\Pi_{3/2}$ level of NO.

dissociation spectrum. In addition to this, between 76725 cm^{-1} and 76775 cm^{-1} (see figure 4.4) the peaks broaden out before being replaced with sharp, narrow peaks that persist to 76900 cm^{-1} (see figure 4.5). It is also worth pointing out that in the ionisation spectrum the intensity in the range 76775-76900 cm^{-1} is generally less than of that in the lower energy range between 76550 cm^{-1} and 76775 cm^{-1} while the opposite is observed in the dissociation spectrum: we generally observe more intense peaks below 76775 cm^{-1} . A note should also be made that while the np(0) and nf(2) series are dominant throughout the spectrum, unambiguous assignment of the ns(1), nd(1) and np(2) Rydberg series becomes difficult after around 76750 cm^{-1} where the

series approximately coincide. This is perhaps unsurprising in the case of the d and s series since they are known to be strongly mixed [69, 70] and this has not been taken into account in the assignment.

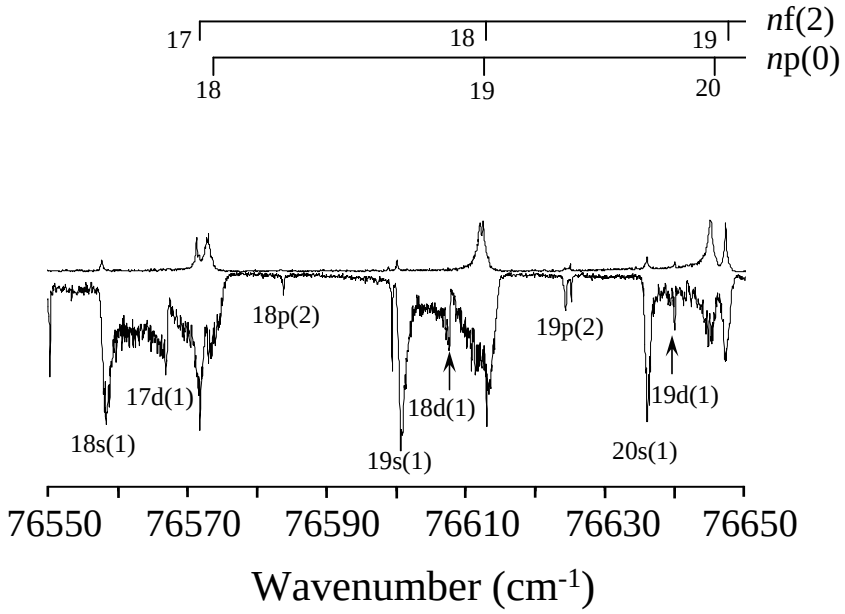

Figure 4.3: Selected region of the spectrum. In the autoionisation spectrum (upper trace) the main features are due to the np(0) and nf(2) series while in the predissociation spectrum (lower trace) there are also large contributions from the ns(1), nd(1) and np(2) series.

The Fano lineprofile is given by

$$R = \frac{(q+\epsilon)^2}{1+\epsilon^2}, \tag{4.2}$$

where q is the shape index and $\epsilon = 2(E - E_n)/\Gamma$ is the reduced energy as defined in section 2.3.3. Γ is the linewidth and is related to the lifetime, τ, through

$$\tau(\text{ps}) = \frac{5.305}{\Gamma(\text{cm}^{-1})}. \tag{4.3}$$

Table 4.1 lists optimised parameters derived from a least-squares fit of equation (4.2) to the experimental data along with lifetimes calculated from equation (4.3). Fits of

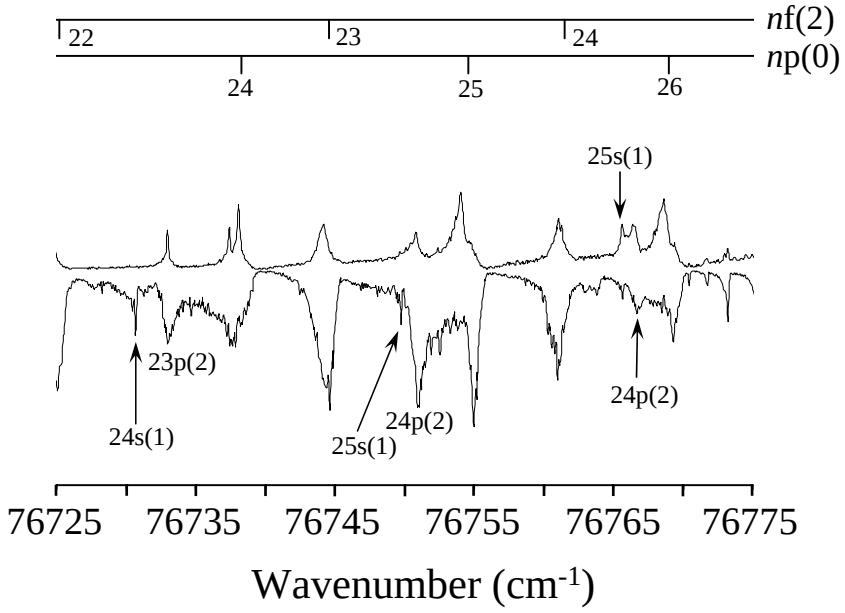

Figure 4.4: Selected region of the spectrum. In this region the autoionising (upper trace) and predissociating (lower trace) resonances are of similar width.

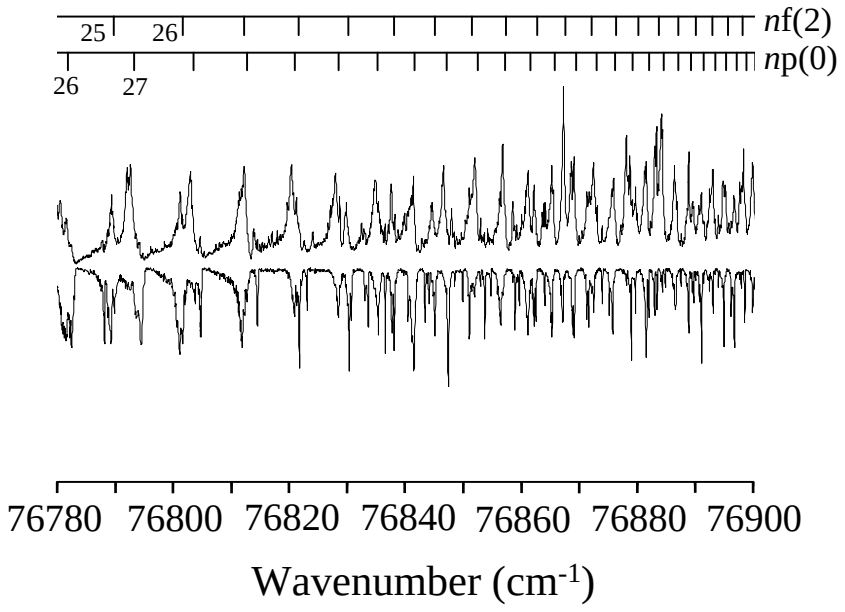

Figure 4.5: Selected region of the spectrum. In this region the widths of corresponding autoionising (upper trace) and predissociating (lower trace) differ widely with the latter exhibiting much sharper lines.

corresponding ionising and predissociating resonances were made in selected regions of the spectrum.

		Autoionisation			Predissociation		
	n	q	$\Gamma(\mathrm{cm}^{-1})$	τ(ps)	q	$\Gamma(\mathrm{cm}^{-1})$	τ (ps)
f(2)	19	32.5	0.35	14.4	-14.9	1.13	4.4
	20	-19.9	0.35	14.4	29.3	0.78	6.5
	21	-17.2	0.38	13.0	-13.5	0.34	14.9
	22	-20.2	0.27	18.6	-21.4	1.57	3.2
	23	-31.1	0.78	6.4	-2.9	1.11	4.5
	24	-13.0	0.78	6.4	-14.0	1.23	4.1
	25	-23.6	0.78	6.4	-11.2	1.15	4.4
	26	-9.8	0.61	8.2	-19.5	0.97	5.2
	27	-8.9	0.42	12.1	-32.7	1.41	3.5
	30	10.0	0.64	7.9	-15.9	0.28	18.0
	31	9.0	0.36	13.9	-6.0	0.16	31.1
	32	-20.6	0.59	8.5	-3.9	0.17	28.9
p(0)	20	-9.3	0.90	5.6	-6.9	1.65	3.0
	21	-9.2	0.73	6.9	-2.0	1.45	3.5
	22	-11.4	0.79	6.3	-3.3	0.99	5.1
	23	-9.1	0.64	7.8	-4.9	1.87	2.7
	24				-1.1	2.19	2.3
	25	-19.4	0.93	5.4	-5.1	0.68	7.3
	26	-17.2	0.95	5.3	-6.3	0.77	6.5
	32	-8.2	1.60	3.1	-9.6	0.56	9.0
	33	13.7	1.12	4.5	-2.9	0.56	9.0
	34	-1.4	0.92	5.5	-3.6	0.69	7.3
	35	-116.6	0.77	6.5	-9.1	0.28	17.8

Table 4.1: Table of parameters derived for selected resonances from the np(0) and nf(2) series from least squares fitting of equation (2.18) to the experimental data. The lifetimes are calculated from equation (4.3). There is no entry for the autoionising 24p(0) resonance since it is affected by an interference (see section 4.2.2)

It is clear from figure 4.2 that resonances belonging to both the np(0) and nf(2) series have distinct asymmetric Fano lineshapes throughout this energy region. With reference to table 4.1 it is apparent that there is a wide spread of shape index, q, although with no discernible trend with principal quantum number. The resonances are, in general, fairly asymmetric and skew to the red ($q < 0$) for the most part. Notable exceptions to this are the 33p(0), 30f(2) and 31f(2) resonances which skew to the blue ($q > 0$) although these occur mostly at higher energies where the density of states becomes large and the Fano formula holds less well. There are two cases at low energy where the skew is opposite, namely the 19f(2) (autoionising) and 20f(2) (predissociating) peaks with $q = 32.5$ and $q = 29.3$ respectively. That said, these flips in asymmetry occur at fairly large values of q indicating an almost symmetric, Lorentzian form. In this case the sign of q becomes less important. Viteri *et al* attributed such flips in asymmetry in BH [89] to interloping (complex) resonances. At this point it is difficult to say whether the observed changes of sign of q are of any consequence and as such a full MQDT calculation would be of use in order to shed light on this. The np(0) series generally have smaller (absolute) values of q than the nf(2) resonances for a given n as indicated by their more pronounced asymmetry.

4.2.1 Lifetimes

Figure 4.6 (a) and (b) plot the lifetime of a given state against the resonance energy for the np(0) and nf(2) series; in both (a) and (b) filled circles indicate a predissociating resonance and open circles autoionising resonances. Below around 76725 cm^{-1} the autoionising lifetime is greater than the corresponding dissociating lifetime for both series with the exception of the 21f(2) peak where the two are similar. Since $\Gamma \propto |V_E|^2$, this indicates that coupling into the dissociative continuum is stronger than that into the ionising continuum in this region of the spectrum. While this is true as a general statement, the magnitude of this difference should be noted; while ionising resonances

of the f(2) series have a lifetime of around 15 ps, their dissociative counterparts have lifetimes of around 5 ps. The difference is less marked in the p(0) series with resonances ionising in around 6.5 ps and dissociating in around 3.5 ps. Another point of interest is that the largest, and smallest, differences between ionising and dissociating lifetimes occur near the same energy for both series, around 76725 cm^{-1} and 76700 cm^{-1} respectively.

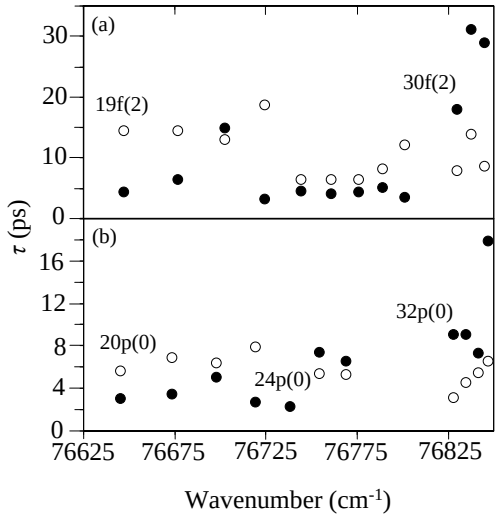

Figure 4.6: Lifetimes for selected members of the (a) nf(2) and (b) np(0) Rydberg series calculated from equation (4.3). Open circles indicate ionising resonances and filled circles predissociating resonances. The energy is referenced to the $X^2\Pi_{3/2}$ level of NO.

In general we observe that across the autoionisation spectrum the np(0) series exhibit shorter lifetimes than the nf(2) series for a given n with the exception of the $n = 23$ peak. There is no such trend for the dissociative resonances; the $n = 20$ and 21 members of the f series have longer lifetimes than corresponding members of the p series whereas for $n > 22$ the lifetimes become similar, to within a couple of picoseconds. Given the nature of the interactions that lead to dissociation and ionisation (*i.e.* the Rydberg electron scattering off the ionic core) one might expect that, for a given n, a more penetrating orbital would exhibit a shorter lifetime than

a less penetrating one belonging to a different Rydberg series[1] and lead us to the conclusion that this is the reason for the generally shorter lifetimes that we observe of the p(0) states relative to the f(2) states. However, the width, and therefore the lifetime, is a measure of the coupling into the continuum and is independent of the quantum defect; if, when comparing Rydberg states belonging to two series with differing orbital angular momentum and therefore having different quantum defects, we note that one has a smaller quantum defect than the other this says nothing about the relative width of a given resonance observed in an experimental investigation. A good example of this is the Rydberg spectrum of Argon which exhibits a very broad d series and a sharp s series (see, for example [92]).

In the small energy range 76725 cm^{-1} to 76800 cm^{-1} there is a notable change in the calculated lifetimes. Lifetimes in both series are similar for ionising and dissociating resonances but while those for the autoionising f(2) states are still larger than the corresponding dissociating states, the converse is true for the p(0) states. It should also be noted that there is a distinct decrease in the ionising lifetimes of the f(2) states from around 15 ps in the lower energy region to around 7 ps in this region. The same decrease is not observed for the dissociating resonances where instead the lifetimes stay approximately steady around 5 ps. Above 76800 cm^{-1} the lifetimes of both Rydberg series have similar behaviour with the dissociative peaks exclusively the longer-lived. There are two other points of note however: firstly, both the f(2) and p(0) series ionisation lifetimes seem to be suppressed in comparison to the dissociative peaks and in fact do not rise, on average, from those in the low energy region. That is to say, throughout this region of the spectrum, the autoionising lifetimes fall into a fairly small range of around 5-15 ps in the case of the f(2) series, and 2-8 ps for the p(0) series. Secondly, the dissociative peaks suffer from no such suppression and rise well above that of lower energies with a maximum lifetime of around 30 ps observed

[1]Of course we restrict this comment to low-l states such as those observed here - the level of penetration into the core region becomes similar very quickly for $l > 3$

in the f(2) series and around 18 ps for the p(0) series.

4.2.2 Interferences

As indicated in section 2.3, the final state distribution in either autoionisation and predissociation from NO is one of $NO^+ + e^-$ or N + O respectively. Both of these may be seen as the result of a scattering of the excited Rydberg electron into a continuum state, be it an ionisation continuum or else some state leading to dissociation of the molecule into atomic constituents. Quite generally in consideration of autoionisation and predissociation then, we can define three states involved in either process: the initial state, $|i\rangle$, the final continuum state, $|j\rangle$, and the excited state lying at the energy of interest, $|E\rangle$. There are then two pathways to the final state distribution

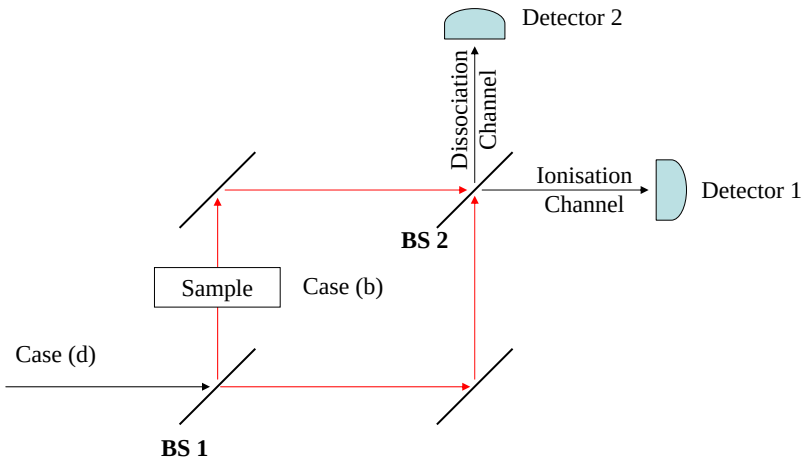

Figure 4.7: Rydberg state dynamics as a Mach-Zender interferometer. The beam of light is the Rydberg electron and each beam splitter represent a frame transformation between Hund's case (b) and Hund's case (d) angular momentum coupling scheme. The sample takes the role of a valence state interaction that induces a phase shift between the two pathways and thus interference between the two decay channels.

and thus interference between the two may occur and a resulting interference pattern

can manifest itself in the spectrum of the molecule[2]. Such interferences also manifest in regions where there are multiple decay pathways available from a given state, in our case the high Rydberg states considered here where both predissociation and autoionisation are available. An analogy in this case may be brought about with reference to a Mach-Zender interferometer (MZI) (see figure 4.7). The input beam of light in the MZI is split at the first beam-splitter (BS1 in figure 4.7). The two beams then propagate through the interferometer and the relative phase of the two beams controls the intensity observed in either output arm of the interferometer. A sample can be placed in one arm of the interferometer to adjust the relative phase between the paths, thus modifying the observed intensity in each of the output arms. In the case of the molecular interferometer then, the Rydberg electron is the beam of light and the first beam splitter takes the role of the frame transformation between a case (d) and a case (b) description of the system *i.e.* where the Rydberg electron has entered into the core region and is scattered into case (b) channels. The sample takes the role of a Rydberg-valence state interaction (or else some other perturbation) that introduces a phase shift between the two pathways in the core region and this phase difference controls the yield that scatters into the case (d) channels as the electron exits the core (inverse frame transformation/beam splitter two.) and thus the relative yields in the dissociation and ionisation channels (detectors one and two). This is, in fact, only a simple two channel system and if we wished to take the analogy further then we would require a further set of 'nested' Mach-Zender interferometers for each of the many available channels in a typical molecular system such as NO. It is clear that a good understanding of such interferences provides a clear insight into the flow of energy within a molecular system and therefore an indication of possible routes for

[2]In fact, this is a qualitative way of understanding the asymmetry in Fano resonances where the interference occurs between direct photoionisation and ionisation *via* the discrete state imbedded in the continuum - changes in the relative amplitudes and phases of the two pathways can then result in a large variation in observed lineshape

coherent control.

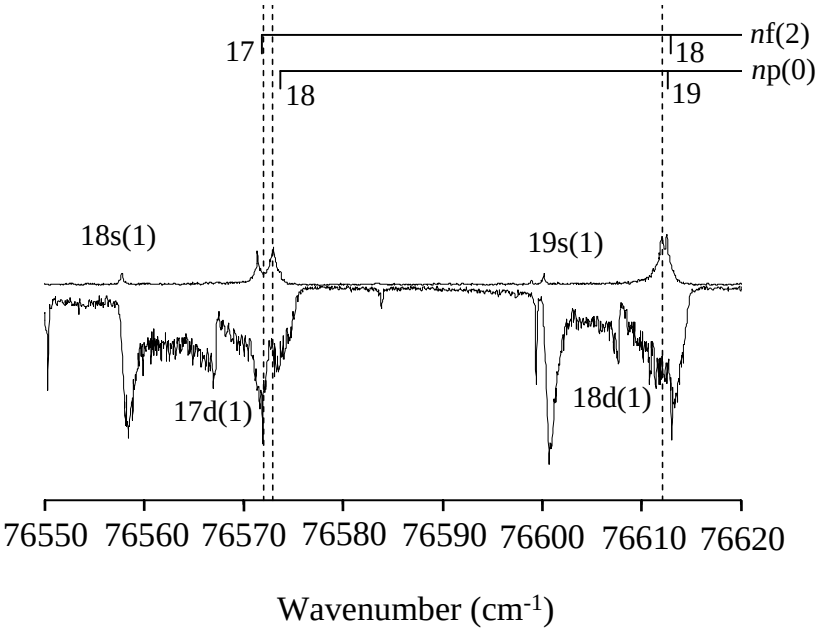

Figure 4.8: Interferences between ionisation (upper trace) and predissociation (lower trace) pathways. The near resonance of the 18p(0) and 17f(2) peaks close to 76575 cm^{-1} cause a maxima in the ionisation/dissociation channel to occur at the same energy as a minima in the dissociation/ionisation channel (indicated by dashed lines). Near 76610 cm^{-1} a peak in the ionisation channel occurs at a broad plateau in the dissociation channel.

Figures 4.8, 4.9 and 4.10 shows specific sections of the experimental spectra where the interplay between the various Rydberg series present have a conspicuous effect on the appearance of the spectrum, in particular leading to preferential decay in one channel and corresponding suppression in one or the other decay channels. Figure 4.8 shows the energy range 76550-76620 cm^{-1} in which the np(0) and nf(2) series are overlapped. Near 76575 cm^{-1} the near resonance of the 18p(0) and 17f(2) states causes a maximum in the ionisation/dissociation channel appearing at a minimum in the dissociation/ionisation channel. Higher in energy, near 76610 cm^{-1} , the relative proximity of the 19p(0) and 18f(2) states results in a peak in the ionisation channel occurring at a broad plateau in the dissociation spectra. In this region there are also

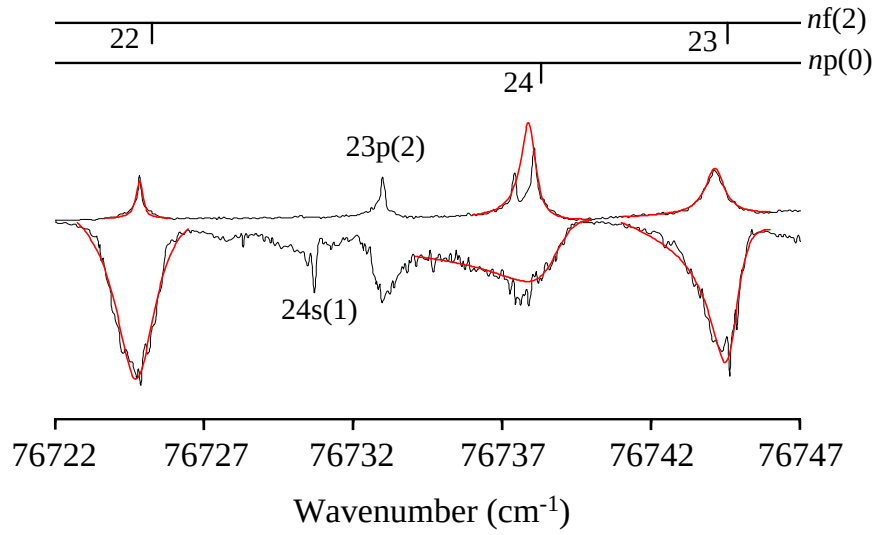

Figure 4.9: Dissociating and ionising decay channels open to the 24p(0) resonance interfere to cause an increased flux through the dissociating channel (lower trace) and a marked decrease in intensity at the ionisation channel (upper trace).

broad, intense features attributable to the nd(1) and ns(1) series.

Figure 4.9 extends over the range 76722-76747 cm^{-1} . The black trace is experimental data while the red curves are the fits of equation (2.18) to the dominant peaks in this region. Here the nf(2) and np(0) lines are approximately interleaved and as such there is little interaction between the two series. However, the weaker nd(1) states are nearly co-incident with the np(0) states here and the effect of this is particularly notable at the 24p(0) resonance near 76738 cm^{-1} ; the ionising peak has a small dip in it and at precisely this energy there is a corresponding additional intensity in the dissociating resonance. This is possibly indicative of some constructive interference in the dissociating channel and destructive interference in the ionising channel.

Figure 4.10 covers the range 76770-76810 cm^{-1} where the 28p(0) and 29p(0) peaks are approximately resonant with the weaker nd(1), ns(1) and np(2) series. The effect of the extra states is dramatic - the intensity of the 28p(0) and 29p(0) states in the

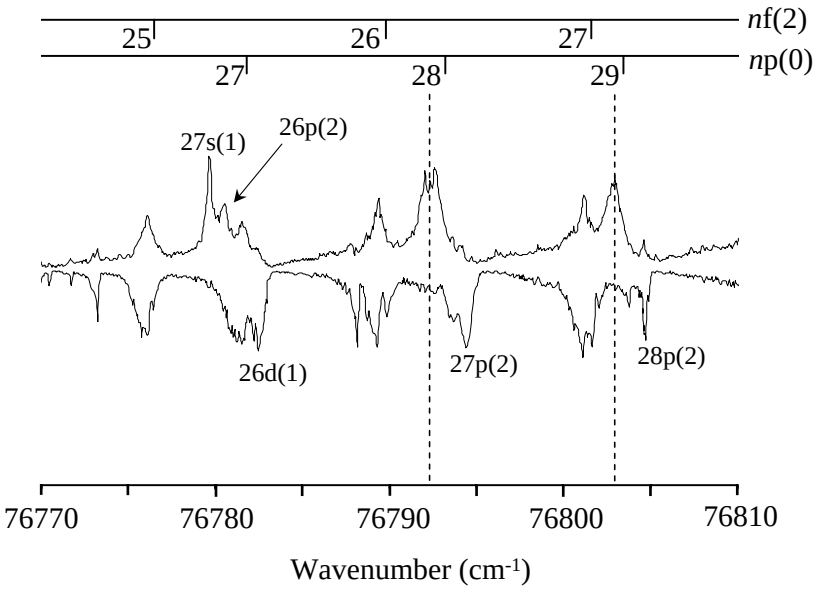

Figure 4.10: The near resonance of the nd(1), ns(1) and np(2) series causes flux to be directed almost exclusively through the ionisation channel (upper trace). The usually dominant np(0) series is now barely present in the dissociation channel (lower trace) and the spectrum is instead dominated by the np(2) and nf(2) series. The dashed lines serve to emphasise the contrast in decay between the channels.

usually dominant dissociation channel is almost entirely removed with almost all of the population now decaying through the ionisation channel. Usually weak, the np(2) now dominate the spectrum along with the nf(2) lines.

4.2.3 The Stroboscopic Effect

With reference to figure 4.6 it is difficult to pick out a particular trend in the lifetimes calculated here. In general one would expect the lifetime to increase in proportion with the orbital period, that is as n^3. Since the decay processes under investigation take place in the core region, a longer period indicates that the Rydberg electron will encounter the core less often over a given period of time and thus the probability of scattering from the core into a continuous state is decreased. However, this deviation

from the atomic-like n^3 scaling is not entirely surprising; NO is a molecular system and as such is vulnerable to perturbations due to the non-spherical core and the vibrating and rotating degrees of freedom the nuclei introduce to the system. That said, the plateau observed in the determined lifetimes of the f(2) states near 76750 cm^{-1} ($\bar{n}_0 \approx 24 - 27$) is reminiscent of earlier work in the group.

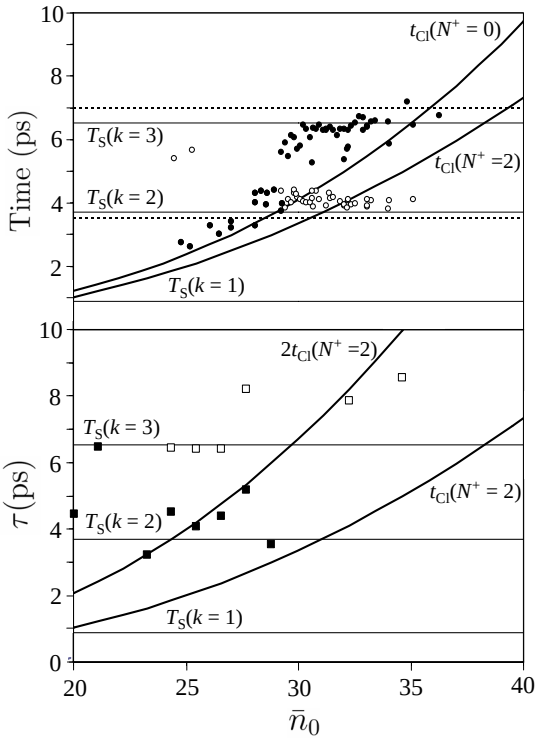

Figure 4.11: (a) Data taken from [1]. Recurrence spectrum as a function of average quantum number in the superposition, $\bar{n}_0$. Filled circles indicate most intense peaks and open circles indicate less intense but still prominant peaks.The wavepackets are excited *via* the $A^2\Sigma^+ |\upsilon' = 1, N' = 0\rangle$ intermediate. Dashed horizontal lines indicate the classical rotational period of a molecular core with $N^+ = 2$; solid horizontal lines indicate the stroboscopic periods, calculated by equation (4.5); solid trend lines mark the hydrogenic periods calculated from $t_{\text{Cl}} = 2\pi\bar{n}^3$. (b) Lifetimes of the nf(2) series from this work. Stroboscopic periods are marked by solid horizontal lines. Open squares indicate ionising resonances and filled squares predissociating resonances. Trend lines mark the first and second hydrogenic periods relative to $\bar{n}_0$.

Figure 4.11 (a) presents data taken from reference [1]. It plots the measured orbital period of a wavepacket in NO excited *via* the $A^2\Sigma^+ |v' = 1, N' = 0\rangle$ against the average principal quantum number of the states contributing to the superposition, $\bar{n}$. As opposed to following simple hydrogenic behaviour, the periods were instead observed to occur at plateaus very close to the classical period of motion of the rotating core. This behaviour was rationalised elegantly by treating the wavepacket as separate electron wavepackets converging to different rotational ionisation limits of the core and evolving along their own trajectory. When the wavepackets overlap spatially they interfere and the resulting interference pattern (*i.e.* the position of the peaks in the recurrence spectrum) is dependent on the molecular phase due to the rotation of the core and the electronic phase which originates from the quantum defect. This phase at the first recurrence is periodic and runs between $-\pi$ to π as a function of average principal quantum number. The phase, ϕ, is given, in atomic units, by

$$\phi = 2\pi\Big(\frac{\mu_{\mathrm{a}}}{t_{\mathrm{Cl}}^{\mathrm{a}}} - \frac{\mu_{\mathrm{b}}}{t_{\mathrm{Cl}}^{\mathrm{b}}} + \frac{1}{T_{\mathrm{Rot}}}\Big)t. \tag{4.4}$$

Here a and b label the Rydberg series converging to lower and upper rotational states of the core respectively. As usual, μ is the quantum defect and t_{Cl} is the orbital period equal to $2\pi n^3$. $T_{\mathrm{Rot}} = 2\pi/\Delta E_{\mathrm{Rot}}$ is the rotational beat period where ΔE_{Rot} is the energy difference between the two ionisation limits. From here a so-called *stroboscopic* period, T_{S}, is derived as

$$T_{\mathrm{S}} = T_{\mathrm{Rot}}(k + \Delta\mu) \tag{4.5}$$

where k is an integer and $\Delta\mu = \mu_{\mathrm{b}} - \mu_{\mathrm{a}}$. Later work took advantage of the phase to achieve optical control of the rotational angular momentum of a molecular wavepacket in NO [38]. A molecular wavepacket composed of a superposition of two non-interacting Rydberg series was excited and, as above, treated as though it consisted of two sep-

arate wavepackets, each with its own electronic orbital angular momentum and associated with different states of the molecular ion, these being separated in energy by ΔE_{Rot}. It was found that optimal control of the system could be achieved if a second wavepacket was launched at a time when the phase was equal to π. This wavepacket was engineered such that it interfered constructively with one Rydberg series and destructively with the other, thus filtering out one component of the superposition and leaving the core in a well-defined rotational state.

We define the energy (in atomic units) of one Rydberg series in terms of another through

$$-\frac{1}{2\nu_{\mathrm{a}}^2} = \Delta E_{\mathrm{Rot}} - \frac{1}{2\nu_{\mathrm{b}}^2} \tag{4.6}$$

where $\nu = n - \mu$ is the effective quantum number. In this way we can plot the accumulated phase difference between the different contributions to the spectrum (*i.e.* the p(0), f(2), d(1), s(1) and p(2) series) relative to a single principal quantum number. The phase was calculated for each combination of Rydberg series excited from the intermediate *i.e.* p(0)-f(2), p(0)-d(1), f(2)-d(1), etc. The pertinant information from the calculations is presented in figures 4.11 (b) and 4.12.

Figure 4.11 (b) is a plot of the f(2) series lifetimes recorded in this work along with the stroboscopic periods for $k = 1, 2$ and 3 plotted on the same scale as 4.11 (a). These were calculated with equation (4.5) using the quantum defects and ionisation limits of the p(0) and f(2) series. Figure 4.11 (b) also has the first and second classical periods of a wavepacket converging to the $N^+ = 2$ ionisation limit and both plots are against the principal quantum number of a wavepacket converging to the $N^+ = 0$ limit; this enables direct comparison of the lifetimes here with the recurrence peaks of [1]. With reference to figure 4.11 (b) we see that several of the ionising f(2) lifetimes lie exactly on the third stroboscopic period. Some of the other dissociative lifetimes lie approximately along the second hydrogenic period and there is generally a fair amount of scatter on the others, both ionising and dissociating. Although far from conclusive,

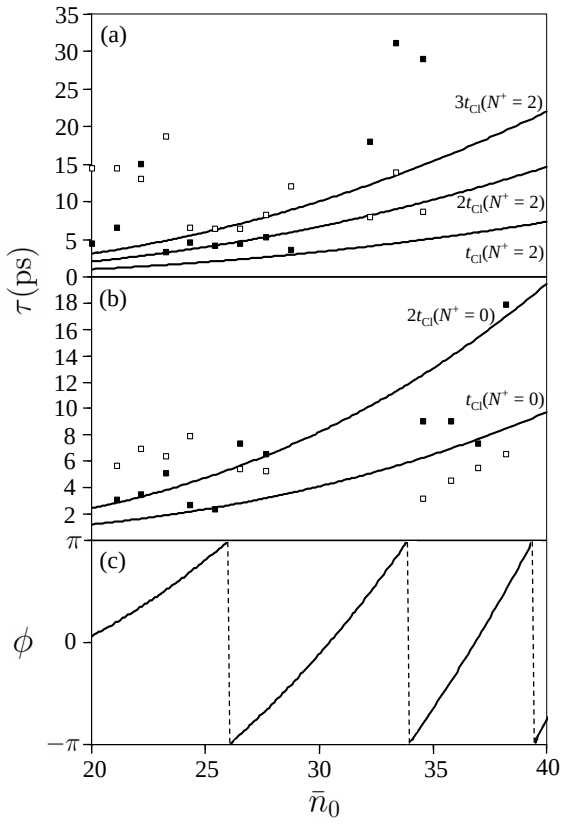

Figure 4.12: Lifetimes calculated in this work plotted against $\bar{n}_0$ for the f(2) (figure (a)) and p(0) (figure (b)) series. Filled squares indicate predissociating resonances and open squares indicate autoionising resonances. (c) The accumulated phase at the first recurrence as a function of $\bar{n}_0$.

the apparent distribution of the lifetimes, and in particular the coincidence of the f(2) states and the stroboscopic period, appears to warrant further investigation in order to see if there is a relationship between the accumulated phase and the lifetimes. For example, given a phase of π at the first recurrence, one would expect diminished population of the Rydberg electron at the core and thus an increased effective lifetime. Figure 4.12 (a) and (b) plot the calculated lifetimes against $\bar{n}_0$ for the f(2) and p(0) series respectively. Figure 4.12 (c) plots the accumulated phase at the first recurrence as a function of $\bar{n}_0$, and the first time that the phase approaches π is near $\bar{n}_0 = 26$. There are two noteworthy points to make here: firstly, it is in this energy region that

the lifetimes of the ionising f(2) series lie on the 3rd stroboscopic period and that the dissociating peaks lie on the second hydrogenic period (see figure 4.11 (b)). Secondly this is very close in energy to the 24p(0) resonance where we see an interference between the ionising and dissociating channels (see figure 4.9). Here we see an increase in flux through the dissociating channel and a corresponding decrease through the ionising channels.

Although an interesting point, it is difficult to say anything conclusive about these results. The p(0) and f(2) Rydberg series are essentially non-interacting and as such it seems likely that any manifestation of an interaction between the two would be where the series lie close in energy; in the region near $\bar{n}_0 = 26$ the p(0) and f(2) series are almost perfectly interleaved. In addition, we see an interference between the fragmentation channels *solely* at the 24p(0) resonance and not in the f(2) series and it also seems unlikely that the phase would have such a distinct and localised effect on only one of the two series involved. While, given figure 4.11 (b), it is clear that the f(2) dissociating lifetimes in the range $\bar{n}_0 \approx 24 - 28$ lie on the second hydrogenic period and the ionising lifetimes in the range $\bar{n}_0 \approx 25 - 27$ lie on the third stroboscopic period, the amount of scatter on the other lifetimes calculated indicate that this may be more due to coincidence than anything else. It is also difficult to rationalise through the stroboscopic effect why the ionising channel would be affected to such an extent while the dissociating resonances retain a certain amount of hydrogenic behaviour; the stroboscopic effect is a consequence of the correlation between molecular and electronic phases and makes no distinction between fragmentation channels. Finally, it should be noted that we see no such correlation, localised or otherwise, between the p(0) series lifetimes and the stroboscopic or hydrogenic periods.

4.3 Summary

Two colour double resonant spectroscopy has been used to examine high-lying Rydberg states of NO above the first ionisation limit where there is competition between autoionisation and predissociation. The spectrum has been assigned where possible and found to consist of contributions from the np(0), nf(2), np(2), ns(1) and nd(1) series. Fano profiles have been fitted to various members of the dominant np(0) and nf(2) series; shape indexes, q, and linewidths, Γ, have been derived thus. Lifetimes have been calculated and a comparison drawn between corresponding autoionising and predissociating resonances. While only a minor contribution to the ionisation spectrum, the np(2), ns(1) and nd(1) series exhibit relatively intense features in the dissociation spectrum; in fact, in opposition to that expected from the propensity rules discussed in chapter 2, in some regions of the spectrum there is a similar contribution from the s(1) states as that from the p(0) and f(2) states.

Both decay channels exhibit a rich variety of lineshapes, widths and corresponding variation in the lifetimes of states. While in general the lineshapes are skewed to the red ($q < 0$) for the majority of resonances, there are occurences of the asymmetry switching and skewing instead to the blue. It is also clear that while for the most part the p(0) states are coupled more strongly to the continuum than the f(2) states, there are also isolated incidents where the converse is true. The many Rydberg series interacting manifest as interferences between the decay channels, in particular causing preferential flux through one channel whilst minimising decay through the other. In some regions this has resulted in almost 100% of the Rydberg population decaying through one channel at the expense of the other. An attempt was made to rationalise the plateau observed in the lifetimes of the f(2) Rydberg states from the perspective of the stroboscopic effect which was unfortunately inconclusive.

The current work serves as preliminary characterisation of the competition between ionisation and predissociation in this region of the spectrum. Further work to

be carried out would be a full MQDT analysis of the region and subsequent comparison of the lineshapes and widths derived from the simple, single discrete state-single continuum model used here with those derived from a multi-channel analysis; a specific point of interest would be how well an MQDT analysis recreates the interferences in the spectrum.

Chapter 5

The effect of vibrational excitation on the predissociation dynamics of the Rydberg states in NO

Above the adiabatic ionisation limit there are still many neutral excited states owing to the vibrational and rotational energy of the molecule; Rydberg states built upon a rovibrationally active core are thus included in this category. The behaviour of such states in diatomic molecules is of interest since, as outlined in previous chapters, they serve both as a model system for the study of non-radiative decay processes and also as a precursor for the design of coherent control schemes in larger, chemically interesting, molecules.

The decay dynamics of Rydberg states lying above the first ionisation limit is influenced not only by the quantum state of the Rydberg electron but also by the rovibrational state of the core. Fujii and Morita's work on NO in the 1990s shed great light on the behaviour of superexcited states in this molecule and revealed numerous complications and subtleties regarding the interplay between the various decay channels available to a molecule lying in a superexcited state. Their work on the competition between rotational autoionisation and predissociation, for example, es-

tablished experimentally that the decay dynamics of superexcited np Rydberg states is governed by predissociation and not by rotational autoionisation [49] and later work established that autoionisation plays the dominant role in determining the decay route for ns Rydberg states lying above the first ionisation limit [52]. Whereas this work probed relatively low energy Rydberg states ($n = 8 - 12$), here we look at the effect of vibrational excitation on the dissociation dynamics of Rydberg states of NO with principal quantum number $n = 18 - 50$. Of particular use when unravelling the dynamics of such states is to compare the spectroscopy and dynamics of states of similar principal quantum number lying above and below the first ionisation limit; in the case of the former, predissociation is the only (non-radiative) decay pathway available whereas for the latter autoionisation also plays a role. Multi-photon excitation to the Rydberg states necessarily probes states of differing rotational quantum number due to the mixed angular momentum character of the intermediate and thus the rovibrational state of the ionic core is likely to impact upon the excited state dynamics. By comparing spectra both above and below the threshold we thus investigate the effect of rovibrational excitation upon the final state distribution.

5.1 Experimental

The experimental setup used to record the $v^+ = 1$ autoionisation and predissociation spectra has been described in detail in chapters 3 and 4. The predissociation spectra from Rydberg states lying below the first ionisation limit were recorded by Nick Jones and Rakhee Patel and have been presented elsewhere (see [60]); that study concentrated on a comparison of the Stark effect in bound and predissociating states. Here we make use of the work below the first ionisation limit to make a comparison between the $v^+ = 0$ and $v^+ = 1$ states. Transitions to the $v^+ = 0$ Rydberg states takes place from the ground $X^2\Pi_{3/2}$ state *via* the $A^2\Sigma^+$ state and as such the propensity rules discussed in section 2.1.3 hold for these states in the same manner as for the $v^+ = 1$ work.

Since we excite from the $A^2\Sigma^+ |\upsilon' = 0, N' = 0, J' = 1/2\rangle$ level we expect the same Rydberg series to be populated as those from the $A^2\Sigma^+ |\upsilon' = 1, N' = 0, J' = 1/2\rangle$ level (albeit being built upon a vibrationless core, of course), namely the np(0), ns(1), nd(1), np(2) and nf(2) series. In particular, due to the angular momentum composition of the A-state (94% s character, 5% d character, 0.3% p character and smaller contributions from other angular momentum states [68, 78]) we expect strong transitions to the p(0) series and only weaker transitions to the np(2) and nf(2) series. Additional, weaker transitions to the ns(1) and nd(1) series are also possible. A Nd:YAG laser operating at 20 Hz pumps two nanosecond dye lasers. The frequency tripled output of the first at 226 nm pumps the $A^2\Sigma^+ |\upsilon' = 0, N' = 0, J' = 1/2\rangle \leftarrow X^2\Pi_{3/2} |\upsilon'' = 0, J'' = 3/2\rangle$ transition to excite to the intermediate state. The frequency doubled output ($\sim$330 nm) of the second laser then scans through the Rydberg states. The main predissociation pathway for the np Rydberg states below the $\upsilon^+ = 0$ threshold is *via* the $B^2\Pi$ valence state to $N(^2D)+O(^3P)$ products (see section 2.3.2) Here decay is monitored into the dominant channel by probing the $N(^2D)$ product in the same way as described in section 2.3.2. The collection of the N^+ product and data acquisition proceeds along the same lines as discussed in sections 3 and 4.1.

5.2 Results and Discussion

In figure 5.1 we present the results of the predissociation measurements of Rydberg states above and below the lowest vibrational state of the ion. Frequency combs mark the unperturbed positions of the p(0), f(2) and p(2) series. The Rydberg states are accessed *via* the $\upsilon' = 0, N' = 0, J' = 1/2$ and $\upsilon' = 1, N' = 0, J' = 1/2$ levels of the $A^2\Sigma^+(3s\sigma)$ state. The similarity in the A-state and Rydberg state potentials facilitates a strong $\Delta\upsilon = 0$ propensity in vibrational transitions and as such the Rydberg states accessed from either the $\upsilon' = 0$ and $\upsilon' = 1$ vibrational state of the intermediate correspond to those converging to the $\upsilon^+ = 0$ and $\upsilon^+ = 1$ ionisation

limits. The spectra are plotted versus their binding energy relative to the rotationless $\upsilon^+ = 0$ and $\upsilon^+ = 1$ ionisation limits of the dominant np(0) series present. This referencing of the energy scale makes it possible to compare states of similar principal quantum number that converge to different ionisation limits.

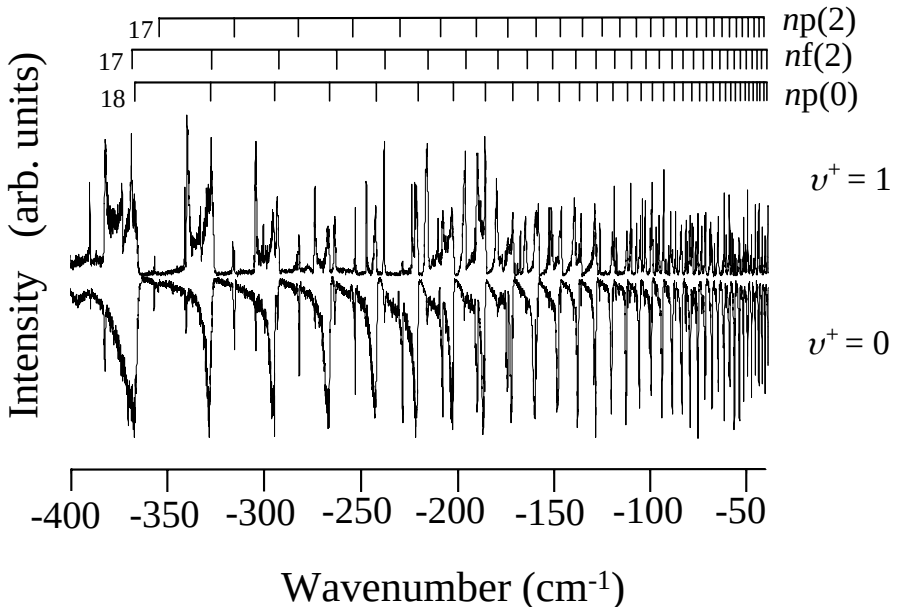

Figure 5.1: Dissociation spectra. Rydberg states converging to the $\upsilon^+ = 1$ (upper trace) and $\upsilon^+ = 0$ (lower trace) dissociate *via* an interaction with the $B^2\Pi$ valence state to form $N(^2D)+O(^3P)$ atomic products. The intensity is plotted against the binding energy of the Rydberg states relative to the $\upsilon^+ = 1, N^+ = 0$ and $\upsilon^+ = 0, N^+ = 0$ ionisation limits corresponding to those of the dominant np series present.

The lower trace in figure 5.1 is the dissociation spectrum recorded from Rydberg states converging to the $\upsilon^+ = 0, N^+ = 0$ ionisation limit. The spectrum shows a set of three main Rydberg series but it is clear that the p(0) series dominates the spectrum with exclusively the most intense and broad peaks. The p(0) series exhibits distinctive Fano lineshapes [81] and the peaks appear relatively unperturbed by the other series present. The p(2) series is strong at low n but with much reduced linewidth and generally lower intensity than p(0) resonances while the f(2) series is also apparent,

though contributing much less intense peaks. The dominance of the p states in the $v^+ = 0$ spectrum is unsurprising - the strong interaction of the p states with the $B^2\Pi$ and $L^2\Pi$ valence states leads to predissociation and has been well documented [16,50]. The most immediately striking feature in the $v^+ = 1$ work is the difference in the appearance of the p(0) series; while still distinct in the $v^+ = 1$ spectrum, this series no longer dominates to the same effect as in the $v^+ = 0$ spectrum. The p(0) states now appear perturbed by the other series having less distinct and regular lineshapes as a result of the impingement of other states. The f(2) peaks are now as strong as the p(0) peaks and the spectrum also has additional strong contributions from the ns(1) and nd(1) peaks while the p(2) series seems to have lost some intensity. The effect of the vibrating core is such that in the low energy region between -350 cm^{-1} and -250 cm^{-1} the s(1) lines now contribute a similar amount to that from the p(0) and f(2) peaks (see figure 5.2) while they are almost absent from the $v^+ = 0$ spectrum.

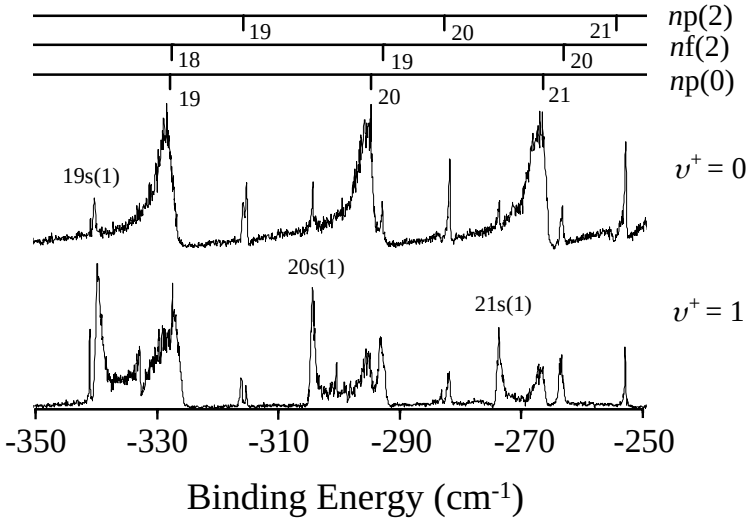

Figure 5.2: Selected region of the spectrum. $v^+ = 0$ (upper trace) and $v^+ = 1$ (lower trace) monitor predissociation into the $N(^2D)$ channel.

Linewidths of the p(0) series for Rydberg states converging to the $v^+ = 1$ and $v^+ = 0$ ionisation limits have been determined by fitting equation (4.2) to the experimental

data; these are presented in figure 5.3. Despite the contrast in appearance of the p(0) series in the two experimental spectra the linewidths for states built on a vibrating ionic core are generally similar to those built on a vibrationless core, particularly as we move to higher principal quantum number. This indicates that vibrational excitation of the core has little effect on the coupling of the p(0) series into the continuum. That said, the linewidths of the p(0)($v^+ = 1$) resonances are significantly smaller than those of the p(0)($v^+ = 0$) resonances for $n = 20, 21, 22$ and 25 which is the region shown in figure 5.4. Here we see that the intensities of p(0) states built on a vibrating core have lower intensities than that of nearby f(2) and s(1) states; the $v^+ = 0$ spectrum, in contrast, is dominated entirely by the p(0) and p(2) states with only minor contributions from the s(1) and f(2) series.

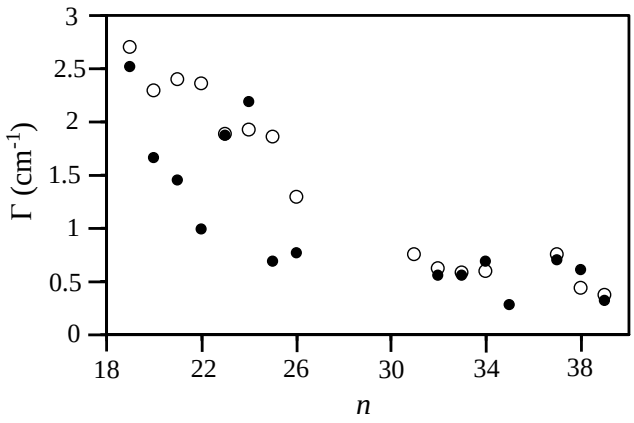

Figure 5.3: Linewidths, Γ, of the p(0) resonances for Rydberg series converging to the $v^+ = 0$ (open circles) and $v^+ = 1$ (filled circles) ionisation limits plotted against principal quantum number, n.

An interesting situation arises in the region -170 cm^{-1} to -130 cm^{-1} (see figure 5.5). Here, the p(0) states still dominate the $v^+ = 0$ spectrum as before but are only a minor contribution to the $v^+ = 1$ spectrum which is now dominated by the p(2) and f(2) states. In fact, this effect is so pronounced that, in contrast to the rest of the spectrum, the 28p(0) and 29p(0) peaks show almost zero decay through the

predissociative channel. We believe this to be a consequence of interplay between the many nearly-degenerate Rydberg series in this region and the point will be discussed shortly with reference to the autoionisation spectrum recorded in chapter 4.

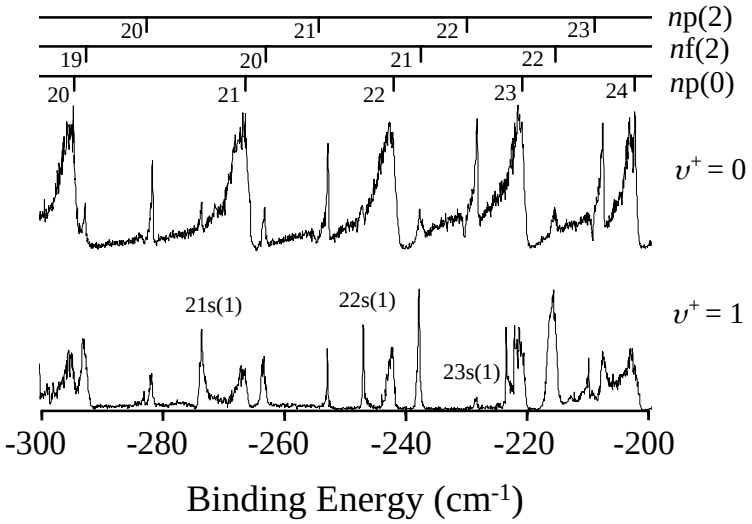

Figure 5.4: Selected region of the spectrum. $\upsilon^+ = 0$ (upper trace) and $\upsilon^+ = 1$ (lower trace) monitor predissociation into the N(^{2}D) channel.

As mentioned above, the similarity between the widths for the p(0) states both above and below the lowest ionisation threshold imply that vibrational excitation of the core has little effect on the predissociation rate for this series. This is clearly not the case for other intense series such as the f(2) and s(1) series which show a marked increase in decay rate upon vibrational excitation. This increase is such that while it was possible to obtain fits for the f(2) series throughout the $\upsilon^+ = 1$ spectrum, only selected members of the f(2)($\upsilon^+ = 0$) series predissociated enough to obtain a quantitative perspective on the relative magnitude of the decay rate above and below the threshold. These were the low energy members of the f(2) series ($n = 19 - 24$) and the fits indicated that vibrational excitation of the core increased the dissociation rate, k, by a factor of around 1.9 with a spread in $k(\upsilon = 1)/k(\upsilon = 0)$ between 3.4 and 0.4.

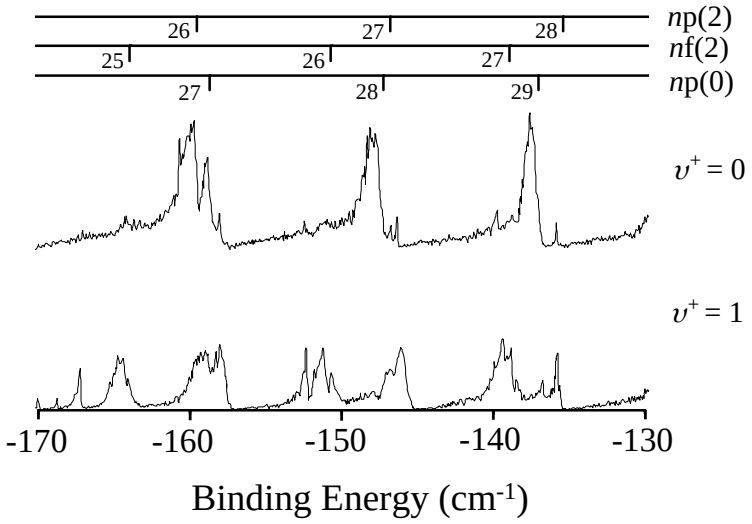

Figure 5.5: Selected region of the spectrum. $\upsilon^+ = 0$ (upper trace) and $\upsilon^+ = 1$ (lower trace) monitor predissociation into the N(^{2}D) channel.

The vibrational excitation also enhances the dissociation rate of the other series that have a rotationally excited core, namely the s(1) and d(1) series, suggesting that coupling to the dissociative states is increased by a rotationally and vibrationally active molecule. The exception to this is the p(2) series. The p(2) intensities are similar to those of the p(0) series at relatively low n but feature much less as we move to higher energies. The comparison between these two series built on a vibrationless core has been made in earlier predissociation experiments in the group [60] and indicates that the intensity of the p(2) states relative to the p(0) states is dependent on the energy separation and ordering. The p(2) series has most intensity for $n = 20 - 26$ where they sit on the low energy side of a p(0) resonance. They are found to be weak or disappear entirely over the range $n = 27 - 45$ where they sit on the high energy side of a p(0) resonance. One possible explanation for this is that the two indirect routes to predissociation (*via* the p(0) and p(2) states) interfere with one another and this interference (constructive or destructive) is dependent on the energy separation and ordering. That said, in this work we monitor only dissociation into the N(^{2}D) channel

and it may be that the p(2) series is more strongly coupled to a different dissociation channel in this energy range. In any case, the p(2) series follows a similar intensity distribution to that observed in the $\upsilon^+ = 0$ work, thus indicating that rovibrational excitation of the core has little effect on this series.

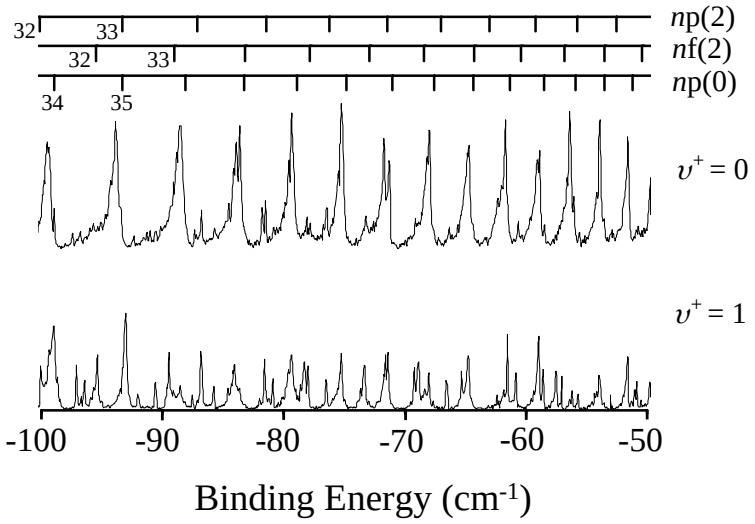

Figure 5.6: Selected region of the spectrum. $\upsilon^+ = 1$ (lower trace) and $\upsilon^+ = 0$ (upper trace) monitor predissociation into the N(^{2}D) channel.

Figure 5.6 compares the spectrum in the energy range -100 cm^{-1} and -50 cm^{-1} . The p(0) series is even more dominant in the $\upsilon^+ = 0$ spectrum as we move to higher principal quantum number with the other series making only minor contributions. In contrast, at high n the $\upsilon^+ = 1$ spectrum is still dominated by both the p(0) and f(2) series and there is evidence of contributions from the other series as well. In this region the widths of the p(0) series are again of similar magnitude thus indicating a correspondingly similar strength of coupling into the continuum as we move to high n.

Below the first ionisation threshold the autoionisation channels are closed and as such there is only one non-radiative decay pathway available to the molecule, namely predissociation. Once we move above this threshold, however, there are both

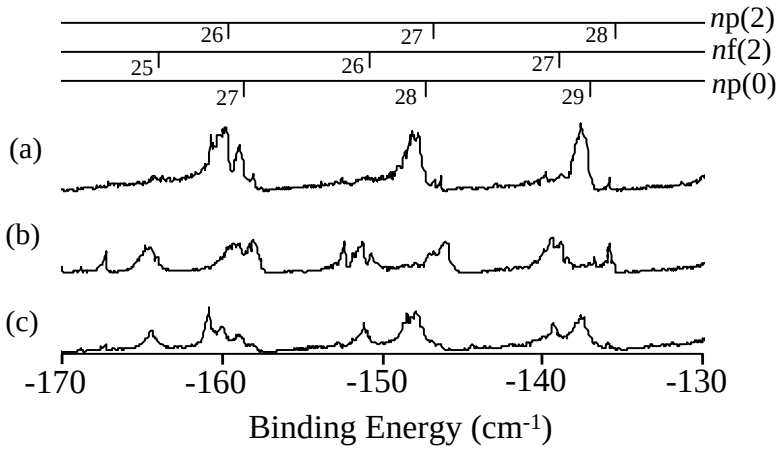

Figure 5.7: Selected region of the spectrum. (a) N(^{2}D) yield spectrum ($\upsilon^+ = 0$). (b) N(^{2}D) yield spectrum ($\upsilon^+ = 1$). (c) Autoionisation spectrum (NO^+ intensity, $\upsilon^+ = 1$).

dissociative and ionising channels open and consequently competition between the two. This competition is highlighted in figure 5.7. Below the first ionisation limit (upper trace) the appearance is very much similar to the rest of the spectrum; the $n = 26, 27$ and 28 members of the p(0) series dominate the spectrum and are broad and intense. The middle trace is the dissociation spectrum from Rydberg states lying above the first ionisation limit. The f(2) peaks are still strong but the p(0) states are now reduced in intensity, almost to nothing in the case of the 27p(0) and 28p(0) resonances. The p(2) states are now fairly intense in contrast to the rest of this spectrum where they make only minor contributions. Finally, the lower trace of figure 5.7 monitors decay into the ionisation channels. The f(2) resonances are strong in this spectrum and the p(0) series is also intense. In this region the s(1), d(1) and p(2) series are near degenerate with the p(0) lines and the effect of this is to force the decay through the ionisation channel at the expense of the dissociation channel.

5.3 Summary

This chapter presents a comparison of the spectroscopy and dissociation dynamics of Rydberg states of NO with principal quantum number $n = 18 - 50$ coverging to the $v^+ = 0$ and $v^+ = 1$ ionisation limits. The below threshold spectrum is dominated by the p(0) series and displays regular, broad Fano lineshapes throughout along with contributions from the p(2) series and weaker contributions from the f(2) series. In contrast the $v^+ = 1$ spectrum is now dominated by the p(0) and f(2) series with additional, strong contributions from the p(2), s(1) and d(1) series. The lineshapes of the p(0) series now appear perturbed by the other states and the intensity distribution is less regular throughout. The effect of the vibrating core is such that in some regions the s(1) peaks contribute a similar amount as that from the p(0) peaks while the f(2) resonances now have similar intensities to the p(0) peaks throughout. The vibrational excitation therefore causes a distinct increase in the coupling to the dissociative continuum for the f(2), s(1) and d(1) series' while the p(0) and p(2) series' appear relatively unaffected. Future work would be to excite from a rotationally active intermediate and examine the extent to which a rotationally active core affects coupling into the dissociative continuum.

Chapter 6

Conclusion

In this thesis, frequency resolved spectroscopy of autoionising and predissociating Rydberg states of NO in the energy region 76550-76900 cm^{-1} above the ground $X^2\Pi_{3/2}$ state are investigated. In chapter 4 two-colour double resonant spectroscopy was employed to examine superexcited Rydberg states converging to the $v^+ = 1$ ionisation limit where there is competition between autoionisation and predissociation. The spectra consisted of contributions from the np(0), nf(2), np(2), ns(1) and nd(1) series. The p(0) and f(2) series were found to contribute strongly throughout the entire energy region of either fragmentation spectrum. However, comparison between predissociating and autoionising spectra revealed that, while the p(2), s(1) and d(1) series made only a minor contribution to the autoionisation spectrum, all three series exhibited relatively intense features in the predissociation spectrum, particularly to lower principal quantum number. Fano profiles were fitted to various members of the dominant p(0) and f(2) series, thus deriving shape indexes, linewidths and lifetimes. Both decay channels exhibit a rich variety of linewidths and shape index and for the most part it is clear that p(0) states are more strongly coupled to the continuum than the f(2) states. An interesting result of this work was the observation of three regions of the spectrum where there are interferences between the autoionising and predissociating decay paths - in some cases this results in almost 100% of the population

decaying through one fragmentation channel at the expense of the other. The above constitutes a qualitative assessment of the experimental data and as such a future study would be a full MQDT analysis of this region of the spectrum and a subsequent comparison between the lineshapes and linewidths derived using this simple, single discrete-continuum interaction, with those from a full calculation. A specific point of interest would be how well such a calculation recreates the interferences and indeed the specific channel interactions involved in order to obtain such a result in the spectrum. It would be interesting to conduct a wavepacket experiment in the vicinity of the interferences to observe how the dynamics are affected. Observation of the dynamics would also serve as the first step towards creating a time-resolved control scheme.

In chapter 5 we make use of earlier work in the group to compare dissociating Rydberg series converging to the $v^+ = 0$ and $v^+ = 1$ ionisation limits. The $v^+ = 0$ spectrum is entirely dominated by the p(0) states, these being both the most broad/short-lived and intense, throughout the whole spectrum. The f(2) states are also present, as are the p(2) and s(1) states, though with much less intensity than the p(0) members. The d(1) series is hardly present at all. Upon vibrational excitation of the core, however, coupling into the continuum is markedly increased in the f(2), s(1) and d(1) series while the p(2) and p(0) series remain relatively unaffected. A further study would be to investigate the effect of a rotationally active core on the dissociation dynamics by exciting *via* a rotationally active intermediate.

Bibliography

[1] R. A. L. Smith *et al.*, Journal of Chemical Physics **119**, 3085 (2003).

[2] T. F. Gallagher, *Rydberg Atoms* (Cambridge University Press, 1994).

[3] T. P. Softley, International Reviews in Physical Chemistry **23**, 1 (2004).

[4] H. H. Fielding, Annual Review of Physical Chemistry **56**, 91 (2005).

[5] I. S. Averbukh and N. F. Perelman, Physics Letters A **139**, 449 (1989).

[6] H. Yasumatsu, K. Tabayashi, and K. Shobatake, Journal of Chemical Physics **104**, 899 (1996).

[7] M. A. Baig *et al.*, Journal of Physics B: Atomic, Molecular and Optical Physics **23**, 3489 (1990).

[8] R. G. Neuhauser, K. Siglow, and H. J. Neusser, Journal of Chemical Physics **106**, 896 (1997).

[9] E. Loginov and M. Drabbels, Physical Review Letters **106**, 083401 (2011).

[10] P. T. Greenland *et al.*, Nature **465**, 1057 (2010).

[11] U. Fano, Physical Review A **2**, 353 (1970).

[12] J.-P. Connerade, *Highly Excited Atoms* (Cambridge University Press, 1998).

[13] C. Greene and C. Jungen, Advances in Atomic and Molecular Physics **21**, 51 (1985).

[14] S. Ross, AIP Conference Proceedings **225**, 73 (1991).

[15] C. Jungen and D. Dill, Journal of Chemical Physics **73**, 3338 (1980).

[16] M. Raoult, Journal of Chemical Physics **87**, 4736 (1987).

[17] K. Ohmori, Annual Review of Physical Chemistry **60**, 487 (2009).

[18] M. Dantus and V. V. Lozovoy, Chemical Reviews **104**, 1813 (2004).

[19] J. A. Fiss, A. Khachatrian, L. Zhu, R. J. Gordon, and T. Seideman, Faraday Discussions **60**, 487 (1999).

[20] C. Chen, Y.-Y. Yin, and D. S. Elliott, Physical Review Letters **64**, 507 (1990).

[21] L. Zhu *et al.*, Physical Review Letters **79**, 4108 (1997).

[22] J. Martin, W. B. Shore, and K. Bergmann, Physical Review A **54**, 1556 (1996).

[23] J. S. Melinger, S. R. Gandhi, A. Hariharan, D. Goswami, and W. S. Warren, Journal of Chemical Physics **101**, 6439 (1994).

[24] R. Sussmann, R. Neuhauser, and H. J. Neusser, Journal of Chemical Physics **100**, 4784 (1994).

[25] D. J. Tannor, S. A. Rice, and P. M. Weber, Journal of Chemical Physics **83**, 6158 (1985).

[26] D. J. Tannor, R. Kosloff, and S. A. Rice, Journal of Chemical Physics **85**, 5805 (1986).

[27] T. Baumert, M. Grosser, R. Thalweiser, and G. Gerber, Physical Review Letters **67**, 3753 (1991).

[28] E. D. Potter, J. L. Herek, S. Pedersen, Q. Liu, and A. H. Zewail, Nature **355**, 66 (1992).

[29] T. Brixner and G. Gerber, ChemPhysChem **4**, 419 (2003).

[30] R. J. Levis, G. M. Menkir, and H. Rabitz, Science **292**, 709 (2001).

[31] N. F. Scherer *et al.*, Journal of Chemical Physics **95**, 1487 (1991).

[32] N. F. Scherer *et al.*, Journal of Chemical Physics **96**, 4180 (1992).

[33] M. W. Noel and C. R. Stroud, Physical Review Letters **75**, 1252 (1995).

[34] M. W. Noel and C. R. Stroud, Physical Review Letters **77**, 1913 (1996).

[35] J. R. R. Verlet, V. G. Stavros, R. S. Minns, and H. H. Fielding, Physical Review Letters **89**, 263004 (2002).

[36] H. Katsuki, H. Chiba, B. Girard, C. Meier, and K. Ohmori, Science **311**, 1589 (2006).

[37] H. Katsuki, H. Chiba, C. Meier, B. Girard, and K. Ohmori, Physical Review Letters **103**, 263004 (2009).

[38] R. S. Minns, R. Patel, J. R. R. Verlet, and H. H. Fielding, Physical Review Letters **91**, 243601 (2003).

[39] R. S. Minns, J. R. R. Verlet, L. J. Watkins, and H. H. Fielding, Journal of Chemical Physics **119**, 5842 (2003).

[40] K. P. Huber, M. Huber, and E. Miescher, Physics Letters **3**, 315 (1963).

[41] E. Miescher, Journal of Quantitative Spectroscopy and Radiative Transfer **2**, 421 (1962).

[42] E. Miescher, Journal of Molecular Spectroscopy **20**, 130 (1966).

[43] E. Miescher, Journal of Molecular Spectroscopy **53**, 302 (1974).

[44] E. Miescher, Y. T. Lee, and P. Gürtler, Journal of Chemical Physics **68**, 2753 (1978).

[45] T. Ebata, Y. Anezaki, M. Fujii, N. Mikami, and M. Ito, Journal of Physical Chemistry **87**, 4774 (1983).

[46] S. T. Pratt, J. L. Dehmer, and P. M. Dehmer, Journal of Chemical Physics **90**, 2201 (1989).

[47] S. T. Pratt, C. Jungen, and E. Miescher, Journal of Chemical Physics **90**, 5971 (1989).

[48] D. T. Biernacki, S. D. Colson, and E. E. Eyler, Journal of Chemical Physics **88**, 2099 (1988).

[49] A. Fujii and N. Morita, Journal of Chemical Physics **98**, 4581 (1993).

[50] A. Fujii and N. Morita, Chemical Physics Letters **182**, 304 (1991).

[51] A. Fujii and N. Morita, Journal of Chemical Physics **97**, 327 (1992).

[52] A. Fujii and N. Morita, Laser Chemistry **13**, 259 (1994).

[53] A. Fujii and N. Morita, Journal of Chemical Physics **103**, 6029 (1995).

[54] M. J. J. Vrakking, Journal of Chemical Physics **102**, 8818 (1995).

[55] R. Patel, N. J. A. Jones, and H. H. Fielding, Journal of Physics B: Atomic, Molecular and Optical Physics **40**, 1369 (2007).

[56] S. R. Mackenzie, E. J. Halse, E. Gordon, D. Rolland, and T. P. Softley, Chemical Physics **209**, 127 (1996).

[57] J. Geng, T. Kobayashi, and M. Takami, Chemical Physics Letters **291**, 277 (1998).

[58] E. F. McCormack, F. Di Teodoro, and J. M. Grochocinski, Journal of Chemical Physics **109**, 63 (1998).

[59] B. B. Clarson, S. R. Procter, A. L. Goodgame, and T. P. Softley, Molecular Physics **106**, 1317 (2008).

[60] N. J. A. Jones, R. Patel, R. S. Minns, and H. H. Fielding, Journal of Physics B: Atomic, Molecular and Optical Physics **41**, 1 (2008).

[61] J. B. M. Warntjes, F. Robicheaux, J. M. Bakker, and L. D. Noordam, Journal of Chemical Physics **111**, 2556 (1961).

[62] A. L. Goodgame, H. Dickinson, S. R. Mackenzie, and T. P. Softley, Journal of Chemical Physics **105**, 7336 (1996).

[63] F. Remacle and M. J. J. Vrakking, Journal of Physical Chemistry A **102**, 9507 (1998).

[64] M. Bixon and J. Jortner, Journal of Chemical Physics **105**, 1363 (1996).

[65] A. Giusti-Suzor and C. Jungen, Journal of Chemical Physics **80**, 986 (1984).

[66] R. Guérout, M. Jungen, and C. Jungen, Journal of Physics B: Atomic, Molecular and Optical Physics **37**, 3057 (2004).

[67] R. E. Stratmann, R. W. Zurales, and R. R. Lucchese, Journal of Chemical Physics **104**, 8989 (1996).

[68] K. Kaufmann, C. Nager, and M. Jungen, Chemical Physics **95**, 385 (1985).

[69] S. Fredin *et al.*, Molecular Physics **60**, 825 (1987).

[70] C. Jungen, Journal of Chemical Physics **53**, 4168 (1970).

[71] M. Hiyama and M. S. Child, Journal of Physics B: Atomic, Molecular and Optical Physics **35**, 1337 (2002).

[72] I. Rabadán and J. Tennyson, Journal of Physics B: Atomic, Molecular and Optical Physics **29**, 3747 (1996).

[73] G. Herzberg, *Spectra of Diatomic Molecules, 2nd Edition* (D. Van Nostrand Company, Inc., 1957).

[74] D. B. Keck and B. C. Hause, Journal of Molecular Spectroscopy **26**, 163 (1968).

[75] G. Herzberg and K. P. Huber, *Molecular Spectra and Molecular Structure, Vol. IV* (New York: Van Nostrand Reinhold Company, 1979).

[76] F. Merkt and T. P. Softley, International Reviews in Physical Chemistry **12**, 205 (1993).

[77] H. Dickinson, D. Rolland, and T. P. Softley, Journal of Physical Chemistry A **105**, 5590 (2001).

[78] S. N. Dixit, D. L. Lynch, and V. McKoy, Physical Review A **32**, 1267 (1985).

[79] M. J. J. Vrakking, Journal of Chemical Physics **105**, 7336 (1996).

[80] R. N. Zare, *Angular Momentum* (Wiley-Interscience, 1988).

[81] U. Fano, Physical Review **124**, 1866 (1961).

[82] P. A. M. Dirac, *The Principles of Quantum Mechanics, 4th Edition* (The Clarendon Press, Oxford, 1967).

[83] P. Brumer and M. Shapiro, Chemical Physics Letters **126**, 541 (1986).

[84] M. Shapiro and P. Brumer, Journal of Chemical Physics **84**, 4103 (1986).

[85] C. Daniel *et al.*, Chemical Physics **267**, 247 (2001).

[86] M. Bergt, T. Brixner, B. Kiefer, M. Strehle, and G. Gerber, Journal Of Physical Chemistry A **103**, 10381 (1999).

[87] V. I. Prokhorenko *et al.*, Science **313**, 1257 (2006).

[88] C. R. Viteri, A. T. Gilkinson, S. J. Rixon, and E. R. Grant, Physical Review A **75**, 013410 (2007).

[89] C. R. Viteri, A. T. Gilkinson, and E. R. Grant, Journal of Chemical Physics **126**, 084301 (2007).

[90] C. Amiot and J. Verges, Physica Scripta **26**, 422 (1982).

[91] H. Rudolph and V. McKoy, Journal of Chemical Physics **93**, 7054 (1990).

[92] H. H. Fielding and T. P. Softley, Journal of Physics B: Atomic, Molecular and Optical Physics **25**, 4125 (1992).